ACES Asian Chemical Editorial Society

doi.org/10.1002/asia.202200170

CHEMISTRY AN ASIAN JOURNAL Review

www.chemasianj.org

Recent Progress on Sb- and Bi-based Chalcogenide Anodes for Potassium-Ion Batteries

Che-Bin Chang and Hsing-Yu Tuan*[a]

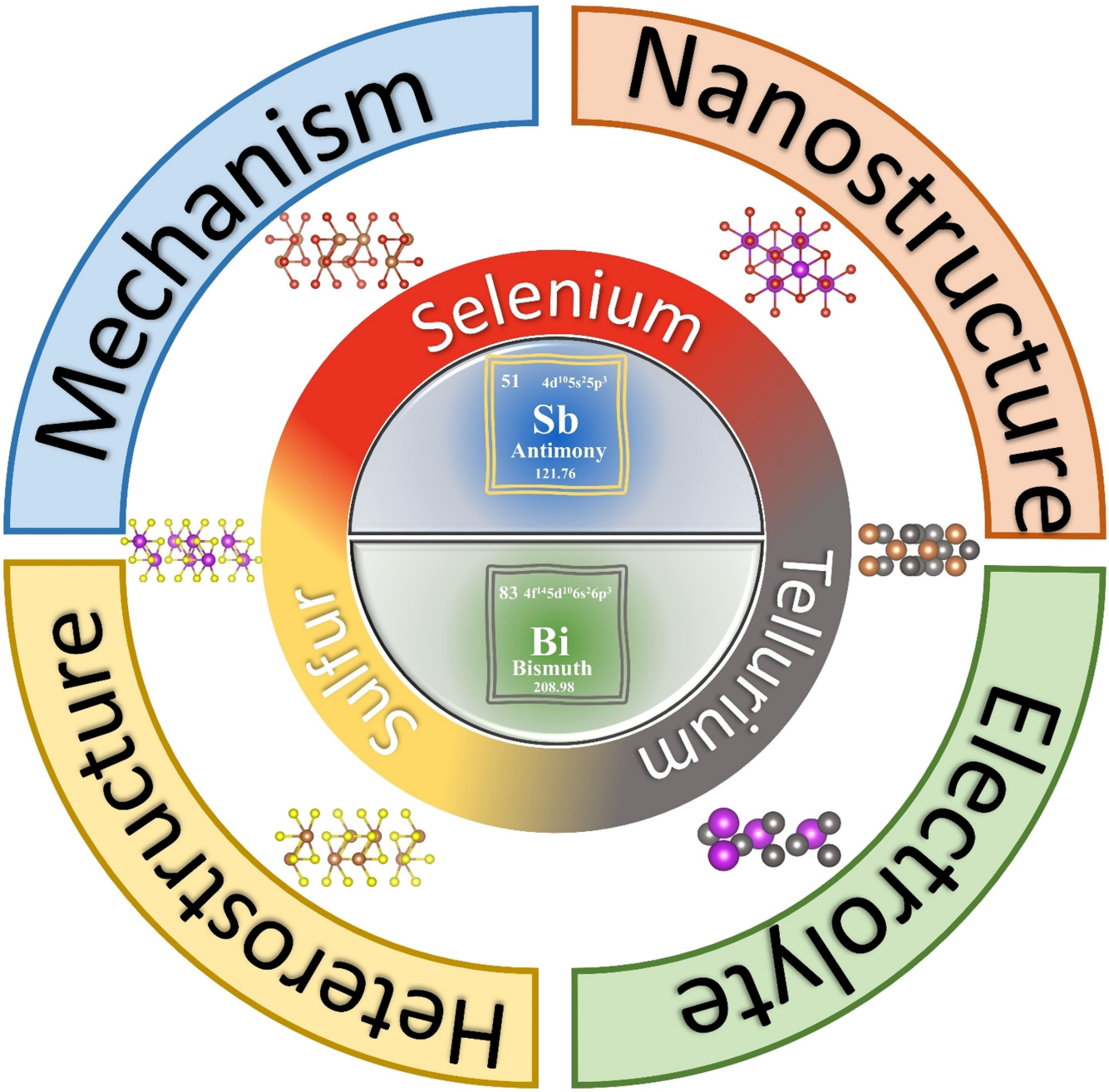

Abstract: Potassium ion batteries (PIBs) are potential alternative energy storage systems to lithium ion batteries (LIBs), due to elemental abundance of potassium, low cost and similar working principle to LIBs. Recently, metal chalcogenides (MCs) have gained enormous interests, especially antimony (Sb)-, bismuth (Bi)-based chalcogenides because they were able to undergo alloying/conversion dual mechanism, which can provide higher specific capacity and energy density ($K_3Sb \sim 660\ mA\,h\,g^{-1}$, $K_3Bi \sim 385\ mA\,h\,g^{-1}$). However, several challenges hinder the development of Sb-, Bi-based chalcogenide anode materials for PIBs, such as huge volume expansion during potassiation, unstable solid-electrolyte interface (SEI), slow reaction kinetics, and polychalcogenide-induced shuttle effect. In this review, the current state-of-the-art Sb-, Bi-based chalcogenides are comprehensively summarized, including the reaction mechanism, electrochemical performance, ingenious nanostructures, electrolyte systems, and prospects for future development. This review contributes to understanding the K^+ storage mechanism and the interaction between active materials and electrolytes, providing guidance and foundation for the design of next-generation high-performance PIBs.

1. Introduction

1.1. Overview of potassium ion batteries

As electric vehicles (EVs) and portable devices development, energy storage technology has faced myriad challenges to satisfy the requirements of high-power, high-energy-density.[1–3] Lithium-ion batteries (LIBs) play a major role in current commercial applications. However, it's urgent to explore another energy storage system, due to shortages and regional distribution of lithium resources making the market price remain high. Potassium ion batteries (PIBs) are a potential alternative energy storage system to LIBs, because of the earth's abundance of potassium sources (17,000 ppm), which is 850 times more than lithium (20 ppm), and similar chemical property with lithium, which allow PIBs sharing alloying, conversion, and intercalation mechanism with LIBs.[4,5] These advantages laying the good foundation of PIBs development. Furthermore, potassium has a low standard redox potential of −2.93 V vs standard hydrogen electrode (SHE), second only to lithium (−3.03 V vs SHE), indicating that PIBs have high operating voltage.[6] Besides, K^+ has a bigger atomic radius resulting in the smallest stokes radius (3.8 Å) between Li (4.8 Å) and Na (4.6 Å), showing that PIBs have better ion conductivity and mobility.[7] Therefore, graphite as a commercial LIB anode material can also be used in PIB, and K^+ intercalation/deintercalation in the graphite layer are highly reversible in the dimethyl ether (DME) system, but the specific capacity and energy density performance are not as good as LIBs, which will be one of the obstacles to the commercial application of potassium-ion batteries.[8,9] Therefore, PIBs anode materials with high theoretical capacity and high cycling stability will be the target.

1.2. Metal Chalcogenides in potassium ion battery

To achieve high power/energy density potassium ion storage technologies, seeking out suitable host materials is crucial to PIBs development.[10] Recently, many researchers invested tremendous efforts to exploit high specific capacity and long cycle life span host materials which can be classified into several categories including intercalation carbon-based materials (graphite, soft carbon, hard carbon, graphene), metal chalcogenides (MCs), metal and metal oxide.[11–17] Among them, MCs with different crystal structure has attracted a lot of attention because of their high theoretical capacity and earth-abundant element resources. MCs, including sulfides, selenides, and tellurides, possess a wide range of properties and are of interest due to their high theoretical capacity and abundant elemental resources on earth.[18,19] Essentially, the M–O bond of metal oxides is much stronger than the M–S bond of metal sulfides, which makes the M–S bond kinetically more favorable for the bond breaking reaction in the conversion reaction and has a higher reactivity.[20–22] In addition, MCs are considered to possess better reaction kinetics, which is attributed to the higher electrical conductivity of K_2S, K_2Se, and K_2Te than K_2O.[23] Therefore, MCs have good reversibility and first cycle efficiency during K^+ storage. According to the different metal elements, MCs can be divided into transition metal chalcogenides (TMDs) and main group metal chalcogenides. The metal components of the former are composed of transition metals, most of which are layered structures (layers bound by van der Waals force).[24] Charge carrier confinement in two dimensions enables efficient electron transfer, offers high tunability, has comparable theoretical capacity, and exhibits smaller volume expansion than alloy materials.[25,26] However, transition metal elements generally do not have K^+ reactivity, which will inevitably lower the theoretical capacity of the material. Therefore, the main group of metal chalcogenides provides a possibility to maximize the theoretical capacity. Both metal and chalcogens elements can contribute capacity, greatly increasing the limits of energy density and power density.

[a] *C.-B. Chang, Prof. H.-Y. Tuan*
Department of Chemical Engineering,
National Tsing Hua University
Hsinchu 30013 (Taiwan)
E-mail: hytuan@che.nthu.edu.tw

1.3. Advantages & challenges on Sb, Bi-based chalcogenides anode materials

Sb and Bi have been developed in LIBs, but due to their low specific capacity (Li_3Sb ~ 660 mAh g^{-1}, Li_3Bi ~ 385 mAh g^{-1}) in comparison with silicon (Si) and phosphorus (P) ($Li_{15}Si_4$ ~ 4200 mAh g^{-1}, Li_3P ~ 2596 mAh g^{-1}), resulting in them receiving little attention in LIBs.[27–30] However, in the PIBs system, traditional elements with high specific capacity (such as Si and P) have less electrochemically activity with K^+, so the final product of the potassiation process does not have the high theoretical capacity (KP ~ 843 mAh g^{-1}, KSi ~ 954 mAh g^{-1}) as in LIB system.[31,32] Therefore, among the active metal elements electrochemically activity in the PIB system, Sb and Bi have great potential, because they have the same theoretical capacity as in the LIB system (K_3Sb ~ 660 mAh g^{-1}, K_3Bi ~ 385 mAh g^{-1}), although the theoretical capacity of the two is still not as high as that of P and Si.[33] However, in the actual electrochemical measurement, the electrochemical performance of Si and P anodes in the experimental data is not as good as the theoretical prediction, only showing about 30% of the theoretical specific capacity, but both Sb and Bi can show the performance close to the theoretical specific capacity (Figure 1).[34,35] Nevertheless, Sb and Bi are more expensive than carbon-based materials, and their content in the earth's crust is relatively scarce.[36] Their higher theoretical capacity means that they suffered larger volume expansion from K^+ storage. The large volume expansion caused by K_3Sb (~ 407%) and K_3Bi (~ 400%) during the potassiation process coupled with the unstable chalcogens conversion reaction will lead to rapid cyclic reversible capacity decay.[37] The low conductivity of the conversion reaction products is a difficult problem for the commercial application of Sb, Bi-based chalcogenides anode materials. In addition, although still in its infancy, Sb, Bi-based chalcogenides can also be applied to different ion storage systems besides the common Li, Na, and K systems, such as zinc-ion batteries (ZIBs) and aluminum-ion batteries (AIBs).[38,39]

Che-Bin Chang received his B.S. degree from the Department of Chemical Engineering, National Chung Cheng University, Chiayi, Taiwan. Currently, he is pursuing a Ph.D. degree under the supervision of Prof. Hsing-Yu Tuan at the Department of Chemical Engineering, National Tsing Hua University, Hsinchu, Taiwan. His research interests include designing and synthesizing nanomaterials and their applications in alkali-ion storage.

Hsing-Yu Tuan received his Ph.D degree in Department of Chemical Engineering from the University of Texas at Austin in 2007. He is now a professor at National Tsing Hua University in Taiwan. His research focuses on nanomaterials synthesis and functionalization, and their applications in the fields of energy storage and conversion.

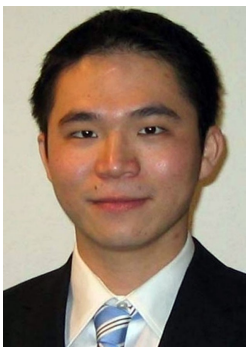

1.4. K-ion Storage mechanism in Sb, Bi-based chalcogenides

Among metal chalcogenides, the potassium ion storage mechanism can be classified into conversion type and conversion/alloying dual type. The conversion type contains electrochemically inactive metal elements (such as Mo, Co, Ni, Fe) for K^+ and chalcogens, Only the reaction between chalcogens and K^+ usually has a simpler reaction mechanism. Because its capacity contribution is mainly contributed by the conversion reaction of chalcogens with K^+, the theoretical capacity is lower than that of the conversion/alloying dual-type mechanism. Thanks to the reaction product of the final potassiation state, the metal element is reduced to a neutral metal phase. The appearance of the neutral metal phase would construct a conductive network, which improved the conductivity and stability of the electrode. The general reaction mechanism of potassiation and depotassiation is shown in equation (1):

$$M_xC_y + yzK^+ + yze^- \leftrightarrow xM + \ldots yK_zC \quad (1)$$

Conversion/alloying dual-type reaction mechanism is contained electrochemically active metals with K^+ (such as Sn, Bi, Sb) and chalcogens. The difference between conversion type and conversion/alloying dual-type is that the metal can react with K^+, which means able to achieve higher theoretical capacity. However, owing to both metals and chalcogens reaction with K^+, putting another instability factor on unstable polychalcogenides redox reaction during potassiation/depotassiation. Although metal elements are alloyed between K^+, higher capacities can be achieved, resulting in dramatic volume expansion that easily leads to pulverization and rapid deactivation of active materials. Furthermore, metal elements didn't remain neutral phase, leading to the poor conductivity of the electrode. The general reaction mechanism of potassiation and depotassiation is shown in equation (2):

$$M_xC_y + (yz + w)K^+ + (yz + w)e^- \leftrightarrow M_xK_w + \ldots yK_zC \quad (2)$$

2. Sb based chalcogenides anode for PIBs

2.1. Sb_2S_3

Antimony sulfide (Sb_2S_3) is the most alternative PIBs materials among metal chalcogenides, because of its high theoretical capacity of 946 mAh g^{-1} in Na^+/Li^+ storage. According to the first Sb_2S_3 mechanism in K^+ storage proposed by Guo's group, it can only deliver 630 mAh g^{-1}, because the final potassiation product is K_2S_3 instead of K_2S.[40] After that, Zhang's group utilized *in-situ* TEM and investigated the reaction mechanism of Sb_2S_3 coating with a carbon layer (Sb_2S_3@C) as shown in

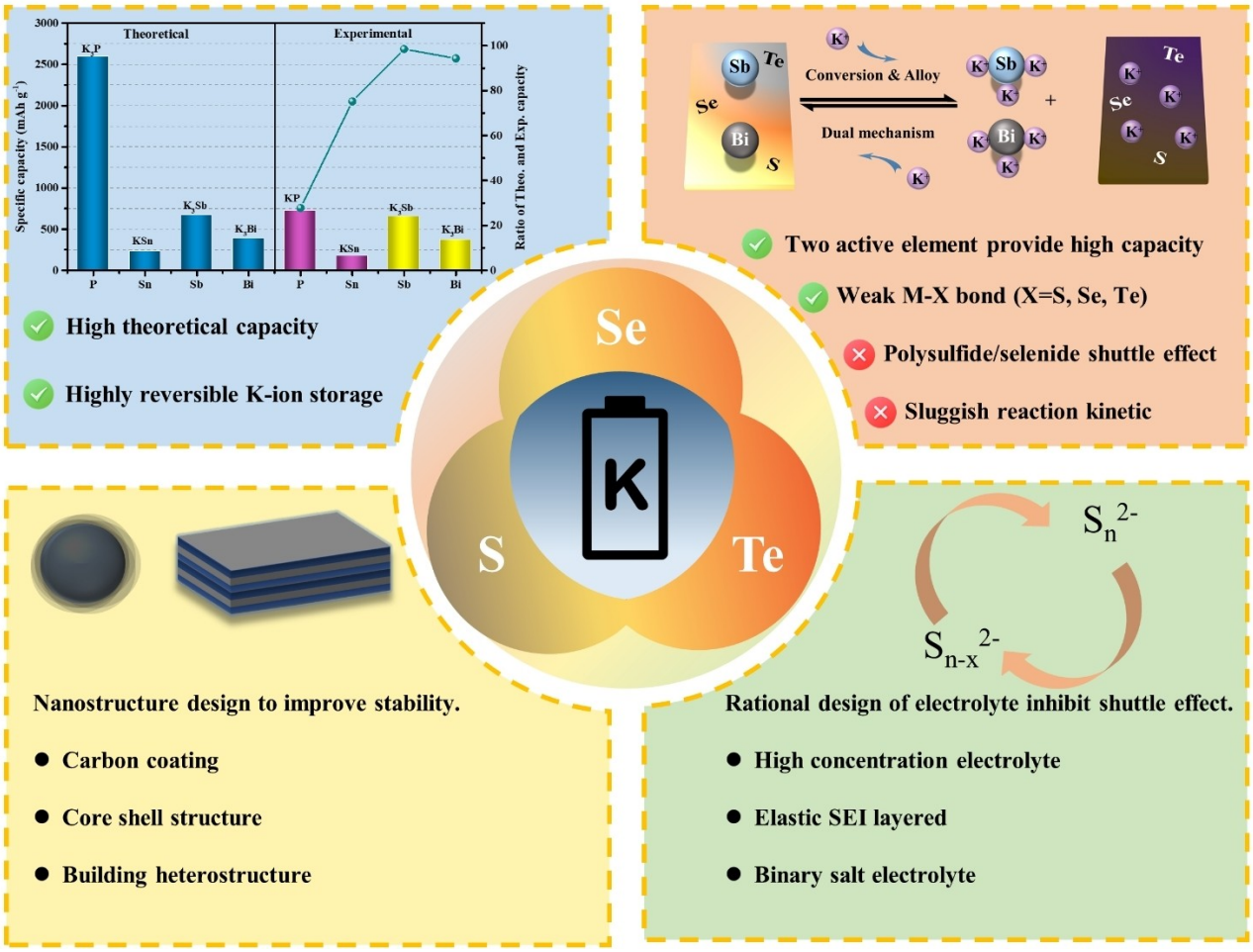

Figure 1. Summary of advantages and challenges on Sb, Bi-Based chalcogenide anodes.

figure 2a–b.[41] Along with the K^+ inserted, Sb_2S_3 diffraction rings have vanished, and diffraction ring of (012) appeared, which index to Sb (PDF# 35-0732) accompanied with amorphous intensity arises. When K^+ inserted continued (185 s) the Sb diffraction rings were disappeared, and four new diffraction rings of KSb (PDF# 42-0791) were detected, which was considered to an intermediate phase of alloying process between K and Sb. Upon reaching the final potassiation state, the intermediate phase of KSb was vanished, and transformed into a final alloying phase of K_3Sb (PDF# 04-0643). It is worth noting that diffraction ring of K_2S also appeared, which has the lowest formation energy in the K–S phases but due to the small size of Sb_2S_3 nanowires that can be fully potassiated to the most stable K_2S phase, the disproportionation of K_2S and K_2S_3 instead of K_2S_2 was not observed in the work ($K_2S_2 \rightarrow K_2S + K_2S_3$). During depotassiation state, the K_3Sb gradually goes through dealloying process ($K_3Sb \rightarrow KSb \rightarrow Sb$) eventually reacted with S (decomposition of K_2S) into the original Sb_2S_3 Phase, but the K_2S suffered from poor reversibility so that the diffraction rings of K_2S still existed in fully depotassiation state.

In Figure 2c, the convert and pristine regions can be easily distinguished, illustrating the potassiation process of Sb_2S_3. Chong *et al.* using *ex-situ* X-ray photoelectron spectroscopy (XPS) (Figure 2d) obtain the peak shift of Sb–S bond to higher bonding energy indicating the conversion reaction.[42] Notably, the converted region containing $K_xS + Sb$ has poor crystallinity which increases the difficulty of analyzing the reaction mechanism between metal chalcogenides with K^+. To better understand what happens between chalcogens and K^+, an analysis method that does not rely on crystallinity should be proposed.

Due to unstable conversion-alloying dual mechanism, various nanostructure which can increase materials stability has been reported. For example, Wang *et al.* reported Sb_2S_3 nanoflower anchored on Ti_3C_2 nanoflakes.[43] The Ti_3C_2 nanoflakes were prepared by etching MAX phases (Ti_3AlC_2) with LiF/HCl and collecting by a freeze drying method. The nanoflakes were further mixed with $SbCl_3$ ethylene glycol solution, and Sb^{3+} would anchor on Ti_3C_2 surface because of negative charge which caused by partial replacement of –O, –OH, –F while etching with LiF/HCl etchant. Sb_2S_3 nanoflowers were synthesized by solvothermal method using thioacetamide (TAA) as sulfur sources as shown in Figure 3a. The formation of Sb–O–Ti covalent bonds was found to indicate a strong interfacial coupling between Sb_2S_3 and Ti_3C_2. Hence, Sb_2S_3–Ti_3C_2 nanocomposite can withstand nearly a specific capacity of 400 mAh g^{-1} at the current density of 100 mA g^{-1}after 100

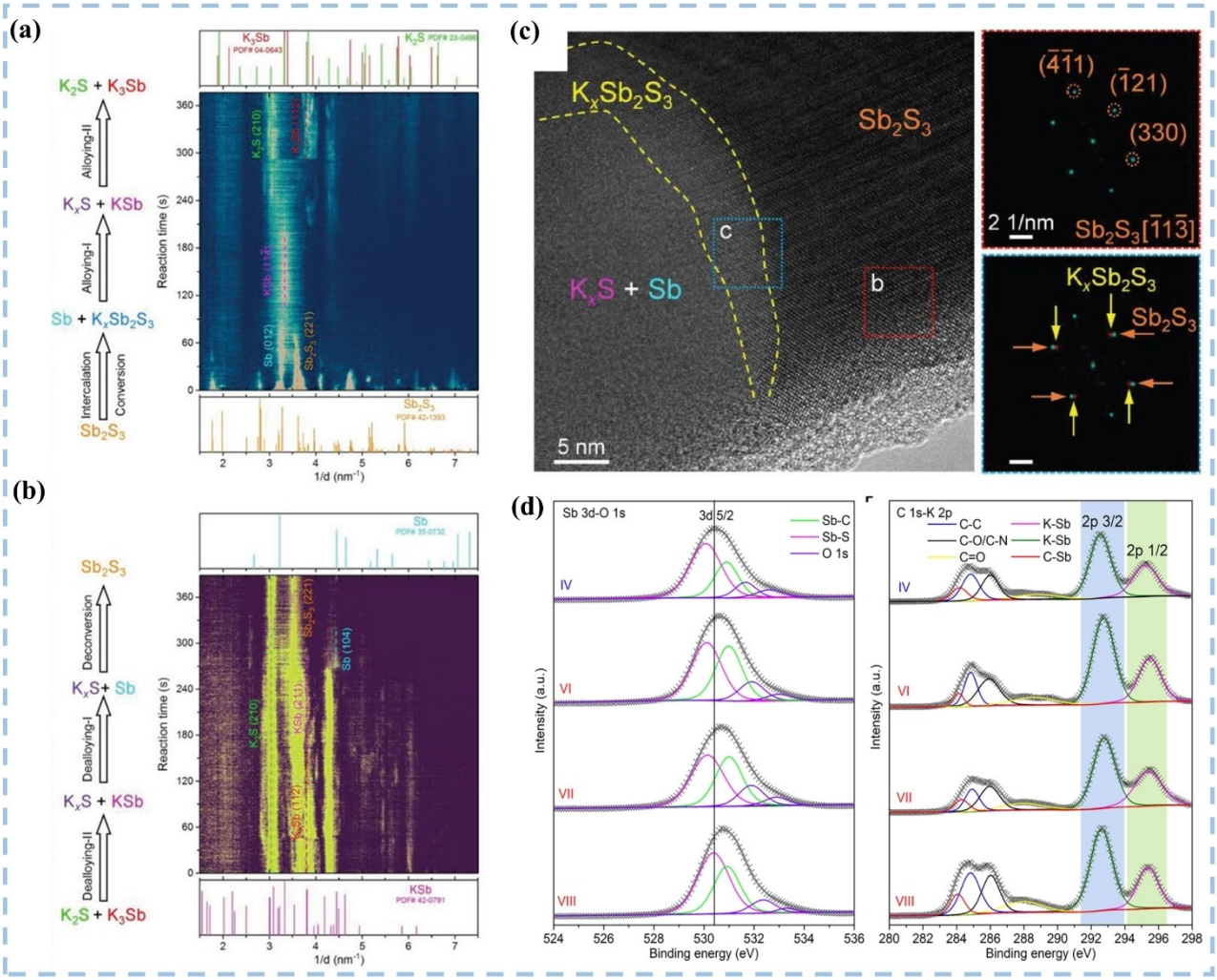

Figure 2. *In-situ* SAED analysis of Sb_2S_3@C NWs during (a) discharge, (b) charge. (c) Evolution of Sb_2S_3@C NWs during potassiation and corresponding FFT patterns. Reproduced with permission.[41] Copyright 2020, Wiley-VCH GmbH. (d) *Ex-situ* XPS of Sb_2S_3@rGO@NC during charge process. Reproduced with permission.[42] Copyright 2021, Elsevier.

cycles, significantly better than individual materials of Sb_2S_3 and Ti_3C_2 (Figure 3b, c). The cycling stability test can also have capacity retention of 79% after 500 cycles. Recently, Shi *et al.* reported polypyrrole (PPy) coated Sb_2S_3 nanorods.[44] The synthesis method was divided into two steps. First, $SbCl_3$ was used as the Sb source, and then mixed with sulfur source followed reacted by a hydrothermal method to generate Sb_2S_3 nanorods. The as-prepared Sb_2S_3 nanorods were put into the solution containing pyrrole monomer, and the uniform PPy coating was formed by the reaction of the oxidant (Figure 3d-i). In Figure 3j, k, Sb_2S_3@PPy has a high reversible specific capacity of 628.1 mAh g^{-1} at a current density of 0.1 A g^{-1}. In the long-term cycling test, it starts to decay after 50 cycles at a current density of 1 A g^{-1}. At the 50th cycle, the specific capacity of 157 mAh g^{-1} remained (Figure 3l, m). There are many ways to coat the functional layer on the surface of the material, such as the PPy mentioned above or the carbon coating layer. For example, Chong *et al.* reported Sb_2S_3 nanorods encapsulated by reduced graphene oxide (rGO) and dopamine induced Nitrogen-doped carbon (Sb_2S_3@rGO@NC).[42] Sb_2S_3@rGO was prepared by one-step solvothermal method, treated with dopamine polymerization, and calcinated at 500 °C to obtain Sb_2S_3@rGO@NC. The nitrogen doped carbon can improve K^+ adsorption and diffusion because of more carbon defects generated. Two carbon layers not only increased the electron conductivity but also buffer the huge volume expansion during potassiation/depotassiation. Sb_2S_3@rGO@NC composite can deliver reversible capacity of 89 mAh g^{-1} after 200 cycles at the current density of 0.2 A g^{-1}, and remained the capacity of 76.7 mAh g^{-1} at the current density of 1 A g^{-1}.

2.2. Sb_2Se_3

The reaction mechanism of the Sb_2Se_3 anode material was first proposed by Yi *et al.* in Figure 4a, b, using Sb_2O_3 coated with resorcinol-formaldehyde (RF) and simultaneously carbonized and selenized to form hollow Sb_2Se_3@C microtubes for electro-

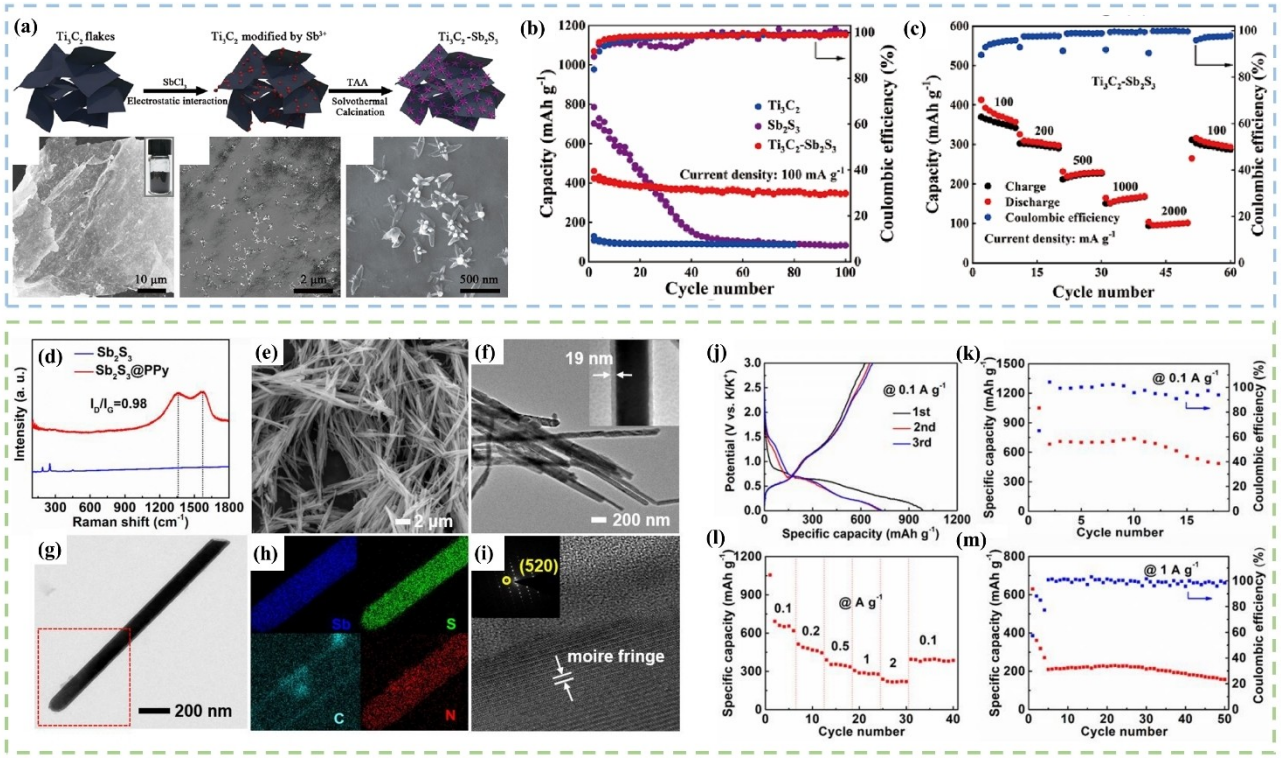

Figure 3. (a) Schematic synthesis procedure of the Ti_3C_2–Sb_2S_3 composite and its morphology. (b) cycling performance of Ti_3C_2–Sb_2S_3 composite, Ti_3C_2, and Sb_2S_3. (c) Rate performance of Ti_3C_2–Sb_2S_3 composite. Reproduced with permission.[43] Copyright 2020, American Chemical Society. (d) Raman spectra of Sb_2S_3 and Sb_2S_3@PPy nanorods. (e) SEM images of Sb_2S_3@PPy nanorods. (f,g) TEM images of Sb_2S_3@PPy nanorods. (h) Element mapping images of Sb_2S_3@PPy nanorods. (i) High resolution TEM (HRTEM) image and selected area electron diffraction (SAED) pattern of Sb_2S_3@PPy nanorods. (j) Galvanostatic charge and discharge curves at 0.1 A g^{-1} for the first three cycles. (k) Cycling stability and corresponding Coulombic efficiency at 0.1 A g^{-1}. (l) Rate capability from 0.1 to 2 A g^{-1}. (m) cycling performance of Sb_2S_3@PPy nanorods. Reproduced from Ref.,[44] under the terms of the CC BY 4.0 license.

chemical testing.[45] *In-situ* Raman was used to analyze the reaction mechanism of Sb_2Se_3@C in potassation/depotassiation. First, strong Raman signals can be found at 187 and 253 cm^{-1} which indexed to Sb_2Se_3 of the original electrode, and the characteristic peaks of Sb_2Se_3 were completely disappeared. Then, new characteristic peaks appeared at 112, 148, and 250 cm^{-1}, which can be assigned to hexagonal Sb. With further K^+ inserted, the peak centered at 148 cm^{-1} has moved to 145 cm^{-1}, which is the result of the alloying process of Sb to K_3Sb. In the discharge process, the formation of K_2Se can be found through *ex-situ* X-ray Diffraction (XRD), but no K_3Sb diffraction peak was be found, indicating the formation of amorphous K_3Sb, and no intermediate phase was observed. Next, the characteristic peaks of K_3Sb gradually shifted to Sb and finally returned to the initial state of Sb_2Se_3 in fully depotassiation state. Subsequently, Sheng *et al.* reported the reaction mechanism of K^+ storage mechanism of carbon-coated and Ni-doped with Sb_2Se_3 using *ex-situ* XPS and Raman.[46] The formation of K_3SbSe_3 phase was observed for the first time during the 1st potassation process, and K_2Se was observed during the gradual discharge state. The generation of K_3Sb phase is consistent with past results. It is worth mentioning that the final product observed during complete depotassization is K_3SbSe_3, rather than returning to the initial state of Sb_2Se_3, which is different from previous reports on the Sb_2Se_3 reaction mechanism and may be related to Ni doping. Recently, Guo *et al.* reported continuous carbon confined Sb_2Se_3 as a PIBs anode material, using *ex-situ* XPS and Raman to analyze the reaction products of a specific potential, revealing that the intermediate phase of KSb_2Se_4 is formed before the final products K_2Se and K_3Sb are formed (Figure 4c–f).[47]

Antimony selenides (Sb_2Se_3) is composed of non-toxic, earth-abundant, and low-cost element, which has narrow bandgap (1.1–1.3 eV), high hole mobility, widely applied in optic and thermoelectric materials. The layered structure of Sb_2Se_3 was grown by $(Sb_4Se_6)_n$ orthorhombic-phase ribbon along [001] stacking with van der Waals force along [010] and [100], and lack of dangling bond to form a heterojunction with other materials. Although Sb_2Se_3 has the less theoretical capacity (669 mAh g^{-1}) than Sb_2S_3 but the final product of K^+ insertion, K_2Se has more conductivity than K_2S. However, Sb_2Se_3 also works in conversion-alloying dual mechanism, which means inevitably unstable chalcogenides conversion reaction and dramatic volume expansion caused by alloying process. Yi *et al.* reported that self-wrinkled rGO confined Sb_2Se_3 nanoparticles composite.[48] Briefly, the self-wrinkled Sb_2Se_3@rGO composite was synthesized using Sb_2O_3@rGO obtained by solvothermal method as precursor further selenization. During selenization process, the self-constriction of rGO could encapsulate Sb_2Se_3 nanoparticles with the rGO more closely (Figure 5h–

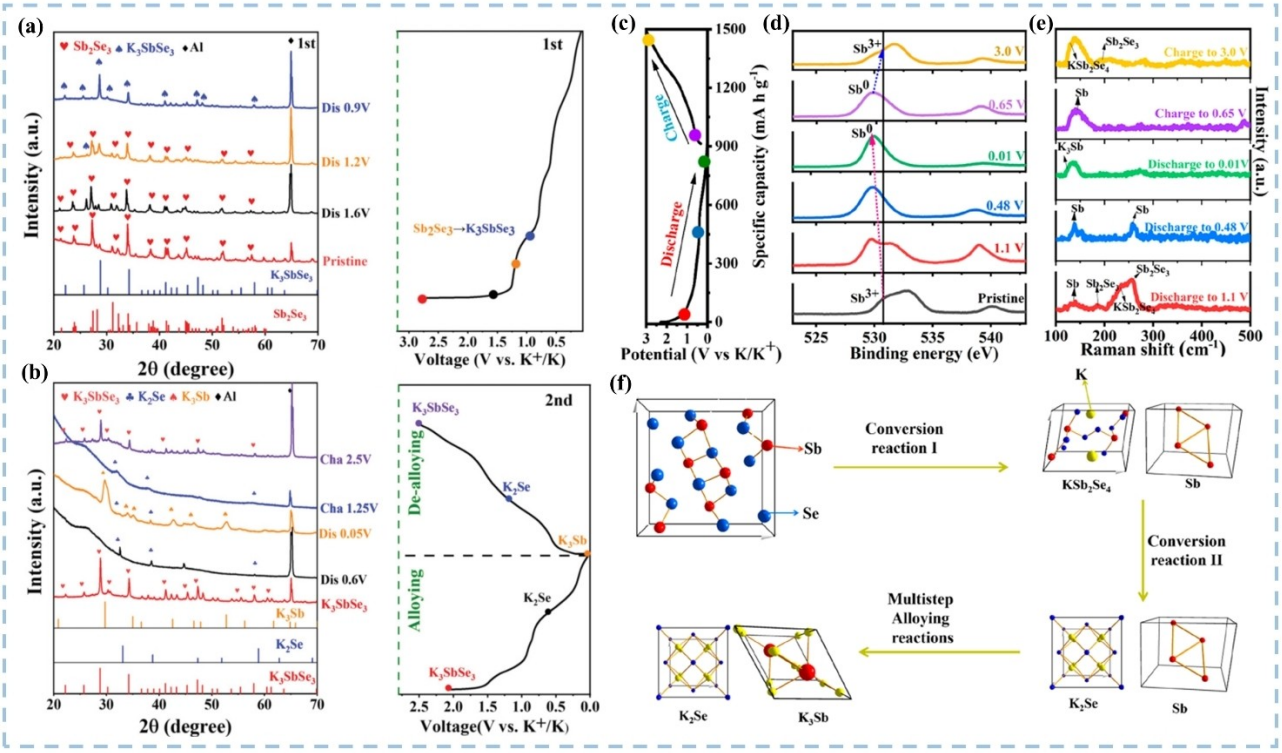

Figure 4. Ex situ XRD patterns and corresponding voltage curve of the $(Sb_{0.99}Ni_{0.01})_2Se_3$@C electrode at (a) 1st discharge process (b) 2nd charge/discharge process. Reproduced with permission.[46] Copyright 2020, Wiley-VCH GmbH. (c) discharge-charge curves at 0.1 A g^{-1}, (d) corresponding ex situ XPS patterns, (e) Raman spectra, and (f) illustration of K^+-storage behavior of C–C/SS electrode. Reproduced with permission.[47] Copyright 2021, American Chemical Society.

k). The self-wrinkles rGO not only provides a mechanical buffer to conquer huge volume expansion during K^+ insertion but also enhances electric conductivity of electrode. Hence, Sb_2Se_3@rGO composites deliver a high reversible capacity of 558 mAh g^{-1} at the current density of 0.05 A g^{-1}, while remaining reversible capacity of 203 mAh g^{-1} after 460 cycles at the current density of 0.5 A g^{-1} (Figure 5m, n). Wang *et al.* further use conductive N-doped carbon and graphene nanosheets double carbon layer confined Sb_2Se_3 nanorods (Sb_2Se_3@NC@rGO).[49] This work shows conductive carbon encapsulation and 2D confinement synergistic effect can effectively suppress pulverization of materials and simultaneously improve the ion conductivity (Figure 5a–d). Both carbon layers form a protective buffer to prevent materials aggregation and maintain the structure construction. Sb_2Se_3@NC@rGO good cycling stability is validated by remaining 250 mAh g^{-1} after 350 cycles at the current density of 0.5 A g^{-1}, while 130 mAh g^{-1} was obtained at the current density of 1 A g^{-1} (Figure 5e–g).

2.3. Sb_2Te_3

Among the chalcogens, elemental Te has the highest electrical conductivity (S: 5×10^{-16} S m^{-1}, Se: 1×10^{-4} S m^{-1}, Te: 2×10^{2} S m^{-1}), which own effective electron transport ability during potassiation/depotassiation process and having high theoretical volumetric capacity of 2621 mAh cm^{-3} to reaching the requirement of nowadays high energy consuming device.[50] Although Sb_2Te_3 has been widely studied on LIBs and sodium ion batteries (SIBs), it still lacks investigation of K^+ storage mechanism and electrochemical performance optimization in PIBs. An in-depth investigation of Sb_2Te_3 anode materials is urgently needed in future work to explore the possibility of novel high volumetric capacity potassium-ion batteries.

3. Bi-based chalcogenides anode for PIBs

3.1. Bi_2S_3

Bismuth sulfide (Bi_2S_3) is a semiconductor material with a narrow bandgap (~1.3 eV) that is commonly used in thermoelectric devices and photodetectors. Notably, Bi_2S_3 has a unique layer structure with weak van der Waals forces, which makes it easier for K ions to intercalate. The inherent properties of Bi_2S_3 make it an ideal anode for PIBs. Although the theoretical capacity is slightly lower than that of Sb-based chalcogenides, its cycle stability is relatively good. Hwang *et al.* deduced the storage mechanism of Bi_2S_3 in PIB based on the previous storage mechanism and DFT of Bi_2S_3 in LIB and NIB.[51] First, Bi_2S_3 will undergo a conversion reaction with K^+ to form metal phases Bi and K_2S, and then metal phase Bi will gradually undergo a transformation reaction. The alloy reacted to form K_3Bi and KBi, and the reaction plates were 1.28, 0.51, and 0.25 V, respectively. Then, Shen *et al.* used *in-situ* XRD, Raman spectroscopy to investigate the storage mechanism of Bi_2S_3. The

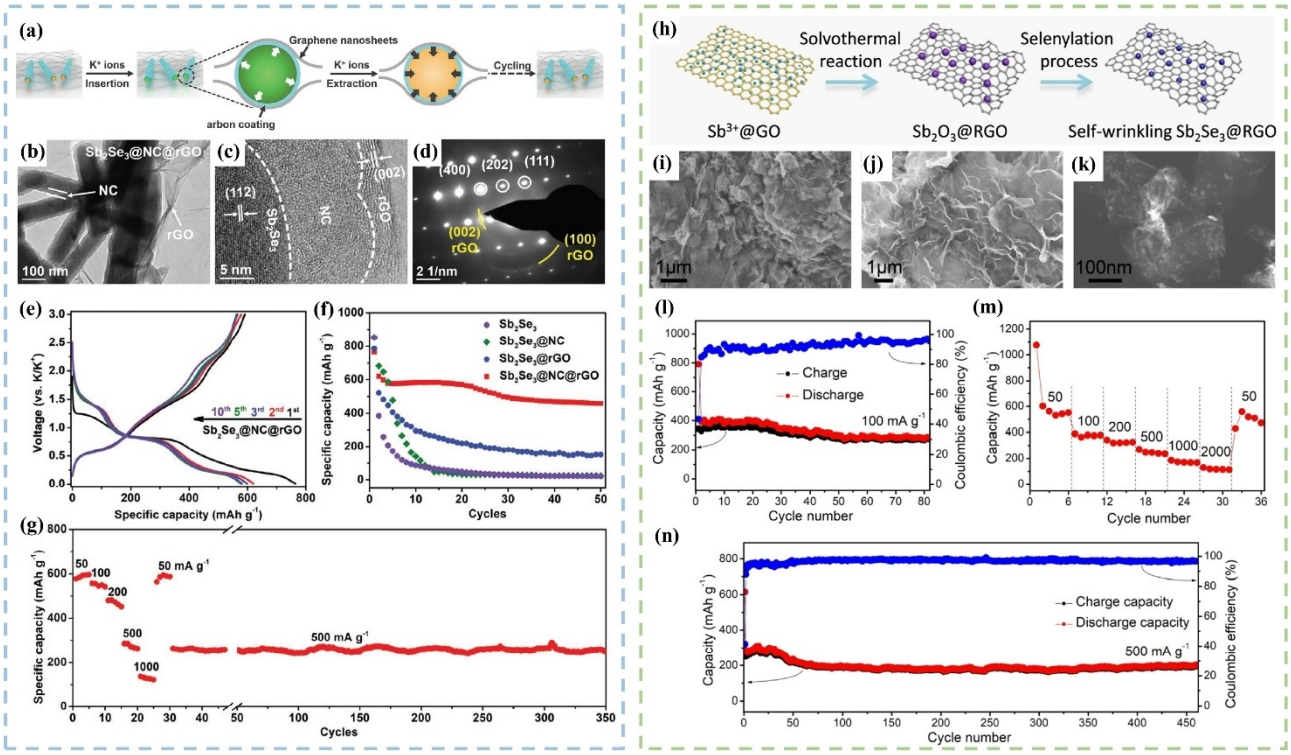

Figure 5. (a) By combining the encapsulation and confinement, both the carbon coating layer and graphene nanosheets help to buffer volume expansion, resulting in well-maintained structural stability within cycling. (b) TEM image of Sb_2Se_3@NC@rGO. (c) HRTEM image of Sb_2Se_3@NC@rGO. (d) SAED pattern of Sb_2Se_3@NC@rGO. (e) GCD curves of the Sb_2Se_3@NC@rGO electrode. (f) Cycling performance of the Sb_2Se_3, Sb_2Se_3@NC, Sb_2Se_3@rGO, and Sb_2Se_3@NC@rGO electrodes. (g) Rate and long-term cycling performances of the Sb_2Se_3@NC@rGO electrode. Reproduced with permission.[49] Copyright 2020, WILEY-VCH. (h) Schematically illustration of the synthetic process of the self-wrinkled Sb_2Se_3@RGO composites. (i) SEM image of the Sb_2O_3@RGO intermediates. (j) SEM image, (k) STEM images of the self-wrinkled Sb_2Se_3@RGO composites. (l) cycling performance of self-wrinkled Sb_2Se_3@RGO composites at 0.1 A g^{-1}. (m) Rate performance of self-wrinkled Sb_2Se_3@RGO composites. (n) long-term cycle stability of self-wrinkled Sb_2Se_3@RGO composites. Reproduced with permission.[48] Copyright 2019, Elsevier.

characteristic peaks of Bi_2S_3 are shifted to a small angle, indicating that the intercalation and conversion reactions are in progress to form $K_xBi_2S_3$.[52] As the state of potassiation deepens, the characteristic peaks of the metal phases Bi and K_2S appear, and then the metal phases Bi and potassium The characteristic peaks obtained from the alloying reaction of ions can correspond to K_3Bi_2 and K_3Bi, respectively, in which K_3Bi is observed as the final product. When charging, K_3Bi_2 and K_3Bi will first undergo depotassiation reaction, reduce to metal phase Bi and undergo reversible conversion reaction with K_2S to generate $K_xBi_2S_3$, S, and Bi phases, and finally return to the original Bi_2S_3 phase, which is speculated by Hwang *et al.* The results are different, and it is the only literature in which element S is observed. More recently, Liu *et al.* used *ex-situ* XRD to observe the characteristic peaks of intercalation and transformation reactions corresponding to $KBiS_2$ (PDF#97-002-8699), followed by the appearance of characteristic peaks of the metallic phase Bi, which also undergoes an alloying reaction with potassium (Figure 6a–c). The same result occurred in in-situ Raman spectra (Figure 6d, e). It is worth noting that the alloying reaction intermediate of Bi with potassium, KBi_2, was observed (Figure 6f). The above reaction mechanisms are consistent with the first-step transformation and intercalation reaction and the stepwise alloying reaction of metallic Bi, but the observed intermediate products are different, which may be attributed to the electrolyte system and the observation method difference.

To overcome the severe volume expansion and unstable conversion reaction caused by the alloying reaction, various functional carbon materials and nanostructure designs were applied in Bi_2S_3 active materials. For example, the heterostructured Bi_2S_3@RGO composite reported by Liu *et al.*, firstly used bismuth nitrate pentahydrate as bismuth source and Thiourea as S source, and prepared Bi_2S_3 microspheres by hydrothermal reaction in ethylene glycol, subsequently proton activated by 3-aminopropyl-trimethoxysilane (APTMS), Then mixed with GO solution via ultrasonic and reduced by vis-light irradiation.[53] Bi_2S_3 was coated with RGO and Bi–O bonds appeared in the XPS spectrometer, indicating that strong chemical force between Bi_2S_3 and RGO, enhanced the mechanical strength of the material and Conductivity, but also increases the contact surface area with the electrolyte (Figure 7a–c). In TEM images (Figure 7d–f), RGO cover on Bi_2S_3 microsphere can be observed clearly. Therefore, Bi_2S_3@RGO composite provides a specific capacity of 250 mAh g^{-1} at a current density of 2 A g^{-1} in the charge-discharge test, while it can cycle for 300 cycles at a current density of 2 A g^{-1} and maintain 237 mAh g^{-1} in the cycle stability test. (Figure 7g). Recently, Wang *et al.* reported Bi_2S_3

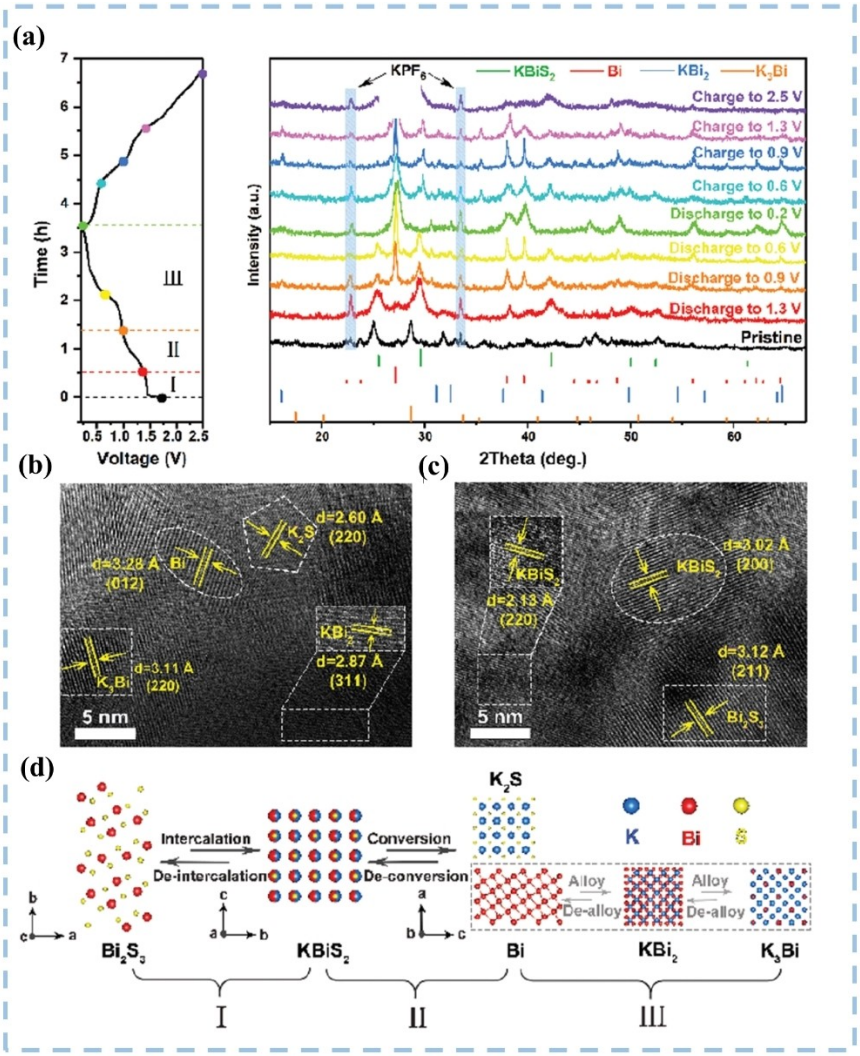

Figure 6. (a) Ex situ XRD patterns of the Bi_2S_3@RGO composite electrode collected during the first electrochemical cycle, with the corresponding charge-discharge profiles on the left. Ex situ HRTEM image of the Bi_2S_3@RGO composite electrode after (b) being discharged to 0.2 V and (c) being charged to 2.5 V. Reproduced with permission.[53] Copyright 2020, Royal Society of Chemistry. (d) Phase evolution of Bi_2S_3@RGO composite during K^+ insertion/desertion. Reproduced with permission.[52] Copyright 2020, Elsevier.

core and sulfur-doped high conductive carbon shell (Bi_2S_3@SC) as active materials of PIB. Bi_2S_3@SC was hydrothermally synthesized by Bi-metal-organic frameworks (Bi-MOFs) as precursors for resorcinol-formaldehyde (RF) coating.[54] Bi-MOFs@RF was obtained, and finally, the Bi_2S_3@SC core-shell structure was obtained by simultaneous sulfide and carbonization in a gas-phase chemical reaction (Figure 7h–k). Due to the high-temperature sulfurization, the carbonized RF also had S doping. The author claimed that S-doped carbon shell not only as a buffer layer but also provides a chemical barrier to inhibit shuttle effect during potassiation/depotassiation. Benefiting from these advantages, the Bi_2S_3@SC core-shell structure delivers specific capacity of 200 mAh g^{-1} at the current density of 0.5 A g^{-1}, while also maintaining 269 mAh g^{-1} at a current density of 1 A g^{-1} (Figure 7l–n).

3.2. Bi_2Se_3

Bi_2Se_3 has a wide bulk bandgap (0.3 eV), a layered structure with weak van der Waals connection, and topological insulator properties, which can lead to new quantum phenomena and devices. They are also highly competitive as potassium ion anode materials, not only due to their considerable large theoretical capacity but also due to the layered structure for high electronic conductivity and facile ionic dynamics. The reaction mechanism of Bi_2Se_3 for K^+ storage was observed by Yang *et al.* using *ex-situ* XRD to observe the initial cycle and make a preliminary explanation.[55] First, the characteristic peaks of Bi_2Se_3 did not change much when discharged from open circuit potential (OCP) to 1.0 V, until 0.5 V, the obvious characteristic peaks of Bi were observed. When reaching the final discharge stage (0.01 V), the characteristic peaks of Bi become weaker, but the characteristic peaks of two common

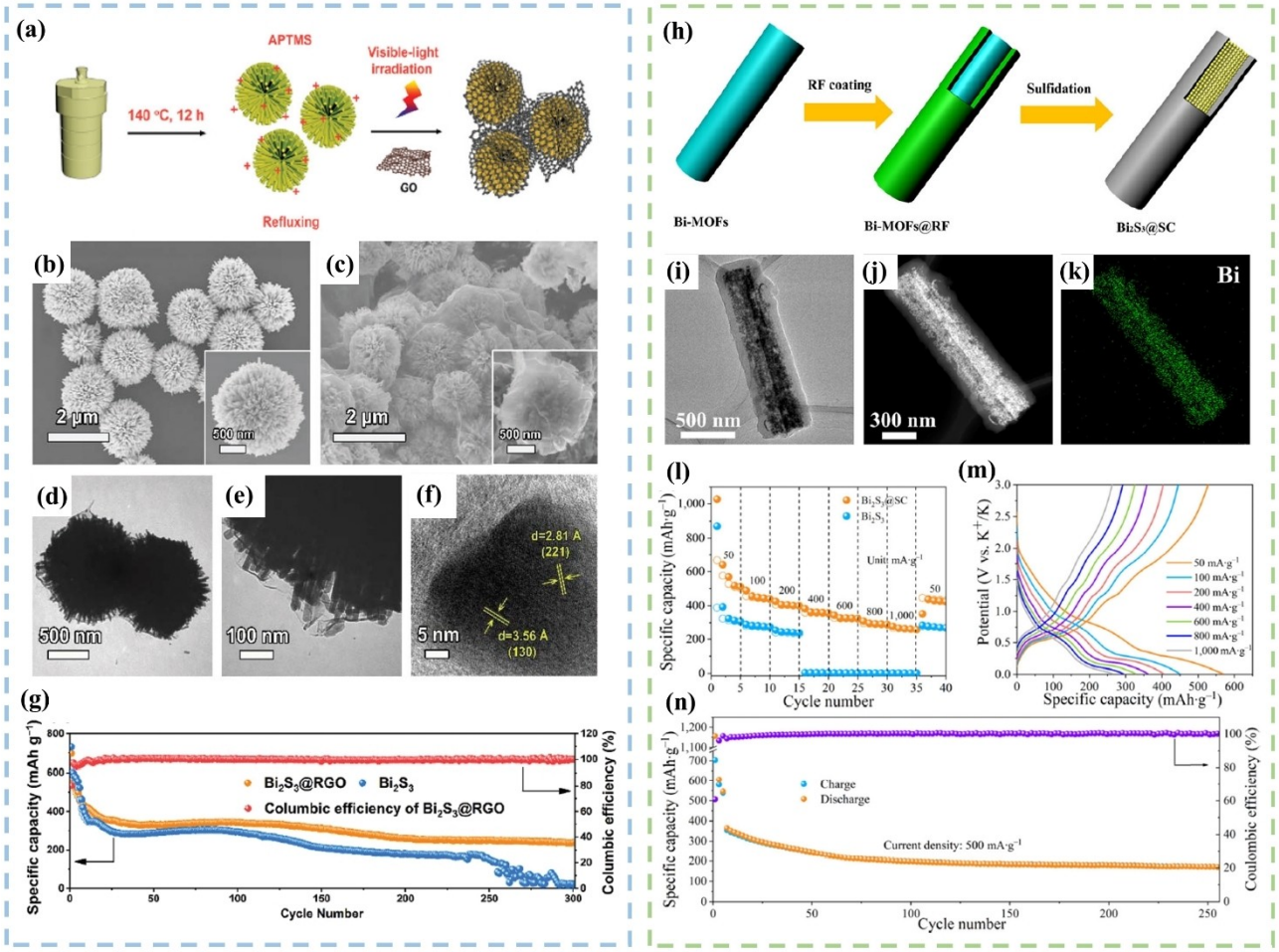

Figure 7. (a) Schematic illustration of the preparation procedure for the Bi_2S_3@RGO composite. SEM image of (b) Bi_2S_3, (c) Bi_2S_3@RGO composite. (d–f) TEM image of Bi_2S_3@RGO composite. (g) Electrochemical performance of Bi_2S_3 and Bi_2S_3@RGO composite. Reproduced with permission.[53] Copyright 2020, Royal Society of Chemistry. (h) Schematic illustration for the synthesis process of the core-shell structured Bi_2S_3@SC. (i-k) TEM images and mapping of Bi_2S_3@SC. (l) Rate performance of Bi_2S_3@SC and (m) corresponding charge-discharge curve. (n) Cycling performance of Bi_2S_3@SC. Reproduced with permission.[54] Copyright 2021, Springer.

final products, K_3Bi and K_2Se, are not observed. During the charging process, the characteristic peak intensity of Bi recovered and finally returned to the fully depotassiation state, and orthorhombic Bi_2Se_3 was observed, which was different from the original rhombohedral phase. Then, Chen *et al.* reported the use of *in-situ* XRD to analyze the energy storage mechanism of Bi_2Se_3 (Figure 8a).[56] From the OCP discharge to 1.0 V, the signal of metallic Bi begins to appear, which is consistent with the results observed by Yang *et al.*, and at the same time, the characteristic peak of K_2Se is also observed, which is attributed to the occurrence of Bi_2Se_3 and K^+ The transformation reaction, it is worth noting that the intermediate phase of the transformation process K_3BiSe_3 was also measured for the first time. Then, with the deepening of the discharge depth, metal Bi and K^+ undergo a typical two-step alloy reaction to form KBi_2 and then K_3Bi in sequence, and the final products are K_3Bi and K_2Se (Figure 8b), respectively. When the charging reaction is performed, K_3Bi will first undergo a step-by-step dealloying reaction and be reduced to metallic Bi, and then undergo the first conversion reaction with K_2Se to return to the K_3BiSe_3 phase and metallic Bi, and then perform the second conversion reaction to return to the initial Bi_2Se_3, the same phase change is reversible in the subsequent second and third measurements, proving its stable two-step conversion-alloy reaction mechanism (Figure 8c).

The bilayer functional carbon structure previously applied to Sb_2Se_3 was also used to stabilize the Bi_2Se_3 active material. Chen *et al.* used Se dissolved in nitric acid as the selenium source, and $Bi(NO_3)_3 \cdot 5H_2O$ dissolved in ethylene glycol (EG) as the selenium source.[56] Bi_2Se_3 nanosheets were prepared by facile hydrothermal method using bismuth source, oleic acid (OA) and Polyvinylpyrrolidone (PVP) were added as surfactants, and then the as-prepared Bi_2Se_3 nanosheet was coated with a layer of polydopamine, and then ultrasonically oscillated with GO. Finally, high temperature calcination is performed to convert polydopamine into N-doped carbon layer, and GO is also reduced to rGO to form Bi_2Se_3@NC@rGO composite (Figure 9a–e). From the BET data, it can be found that the overall specific surface area is higher than that of the non-carbon material coating. is about 3 times higher, which provides better

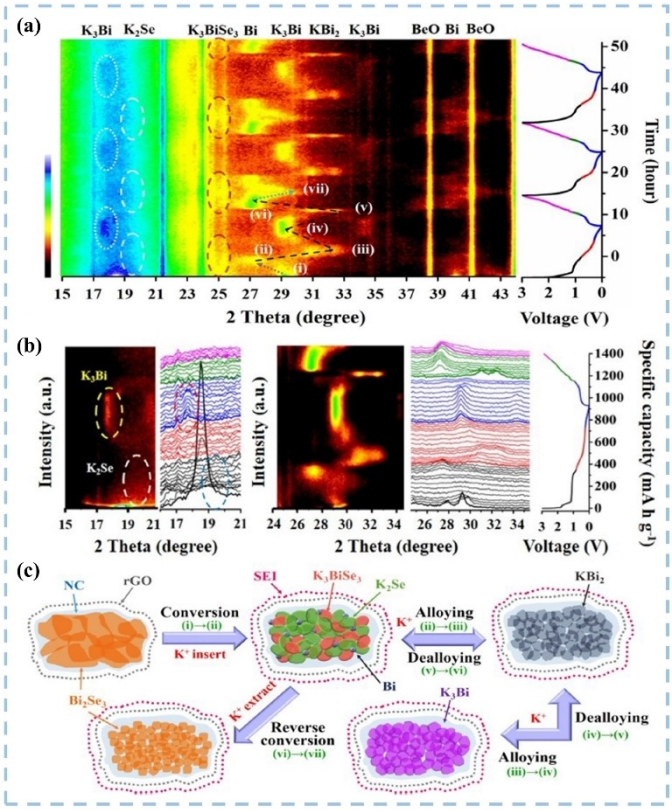

Figure 8. (a) In situ contour plot of the operando XRD result of Bi_2Se_3@NC@rGO electrode during the K-ion insetion/extraction process of the initial three cycles. (b) In situ XRD patterns and corresponding line plots of Bi_2Se_3 electrode. (c) schematic view of the proposed electrochemical mechanism during the charge/discharge process. Reproduced with permission.[56] Copyright 2021, Elsevier.

reaction contact area and buffer volume, which is beneficial for K^+ storage. Therefore, Bi_2Se_3@NC@rGO composite achieved the highest specific capacity at each current density in the control group in the rate performance test and provided a specific capacity of 102 mAh g^{-1} when the current density was 5 A g^{-1}, while it can also maintain a reversible capacity of 114 mAh g^{-1} after 1000 cycles of cyclic reaction (Figure 9f–h). Subsequently, Yang *et al.* used Benzenetricarboxylic acid and bismuth nitrate pentahydrate in methanol for hydrothermal reaction to prepare Bi-MOF, followed by one-step chemical vapor phase reaction for carbonization and selenization to obtain Bi_2Se_3@C composite.[55] It is worth noting that during the selenization process, the existence of the ligand in Bi-MOF will lead to the appearance of porous carbon materials during the selenization process, and the mesoporous characteristics are obtained in the BET test. Bi_2Se_3@C composite can maintain specific capacity of 304 mAh g^{-1} at the current density of 2 A g^{-1} (Figure 9f–m). The specific capacity can still be maintained at 543 mAh g^{-1} after 5000 cycles at a current density of 1 A g^{-1} (Figure 9n). Zhao *et al.* also uses Bi_2Se_3 nanosheets as active materials but coated with different carbon layers.[57] Bi_2Se_3 nanosheets are also prepared by hydrothermal method, but the source of carbon layers is glucose. Because there is no nitrogen in the glucose molecule, thus forms an undoped carbon coating, resulting in Bi_2Se_3@C (glucose derive). Bi_2Se_3@C (glucose derive) can maintain the reversible capacity of 210 mAh g^{-1} at a current density of 2 A g^{-1} and can still maintain the capacity of 214 mAh g^{-1} after 1000 cycles at a current density of 1 A g^{-1}.

3.3. Bi_2Te_3

Bismuth telluride (Bi_2Te_3) allows electrons to be exclusively and freely transported along the two-dimensional surface of the material. Compared with Bi_2S_3 and Bi_2Se_3, Bi_2Te_3 has higher electrical conductivity and interplanar spacing, and has a very considerable volume capacity. Potential PIB anode material. However, there are relatively few reports on Bi_2Te_3. The K^+ storage mechanism of Bi_2Te_3 was first proposed by Gillard *et al.* using *ex-situ* XRD.[58] When K^+ inserts into Bi_2Te_3, the characteristic peaks of Bi_2Te_3 gradually change. It is speculated that $K_xBi_2Te_3$ is formed until 45% of potassiation state. As the degree of potassiation deepens, K_2Te_3 transforms into K_2Te_5, and the metallic phase Bi transforms into K_2Bi. The phase change during charging is not discussed in the literature. Subsequently, Ko *et al.* used *in-situ* XRD and X-ray absorption near-edge structure (XANES) spectroscopy to observe the charge-discharge phase changes of Bi_2Te_3 (Figure 10a).[59] When the discharge reached 0.85 V, the characteristic peak of the metallic phase Bi gradually appeared, but no characteristic peak of K and Te was observed. According to the final products in Bi_2S_3 and Bi_2Se_3, it is possible to form amorphous K_2Te. As the voltage gradually decreases, the metal phase Bi undergoes a typical alloying reaction and the final product of K_3Bi is generated, which through interphase of KBi_2 and K_3Bi_2. The in-situ XRD result can also index HRTEM image and SAED pattern in corresponding voltage. When in depotassiation process, the voltage charged to 1.0 V, the characteristic peaks of K_3Bi gradually disappeared and were replaced by the characteristic peaks of KBi_2. Finally, charging to 2.0 V, the characteristic peaks of Bi_2Te_3 reappeared and entrainment with a small amount of metallic phase Bi. In XANES spectroscopy (Figure 10b, c), the change of the valence of Bi from 0 to 3^+ is observed, which corresponds to *in-situ* XRD result. but the change of the valence of Te always maintained at 2^-. The authors claim that Te as Te^{2-}, is inactive in PIB. The overall reaction mechanism can schematically shown in Figure 10d.

Ko *et al.* used $BiCl_3$ and Na_2TeO_3 as bismuth source and tellurium source and made Bi_2Te_3 powder by hydrothermal reaction with EDTA and $NaBH_4$. Subsequently, Bi_2Te_3@C was obtained by high-energy ball milling (350 rpm) between Bi_2Te_3 and acetylene black.[59] After high-energy ball milling with acetylene black, not only the average particle size of Bi_2Te_3 is reduced, but also the conductivity is improved. It can be clearly observed from the TEM image that the surface of the Bi_2Te_3 is covered with a layer of carbon material. As we know, the reduce of the average particle size can prevent the pulverization of the active material, and the coating of the carbon layer not only provides a buffer zone for the volume expansion induced by potassiation/depotassiation process, but also improve the rate performance. The more stable CV curve were shown in

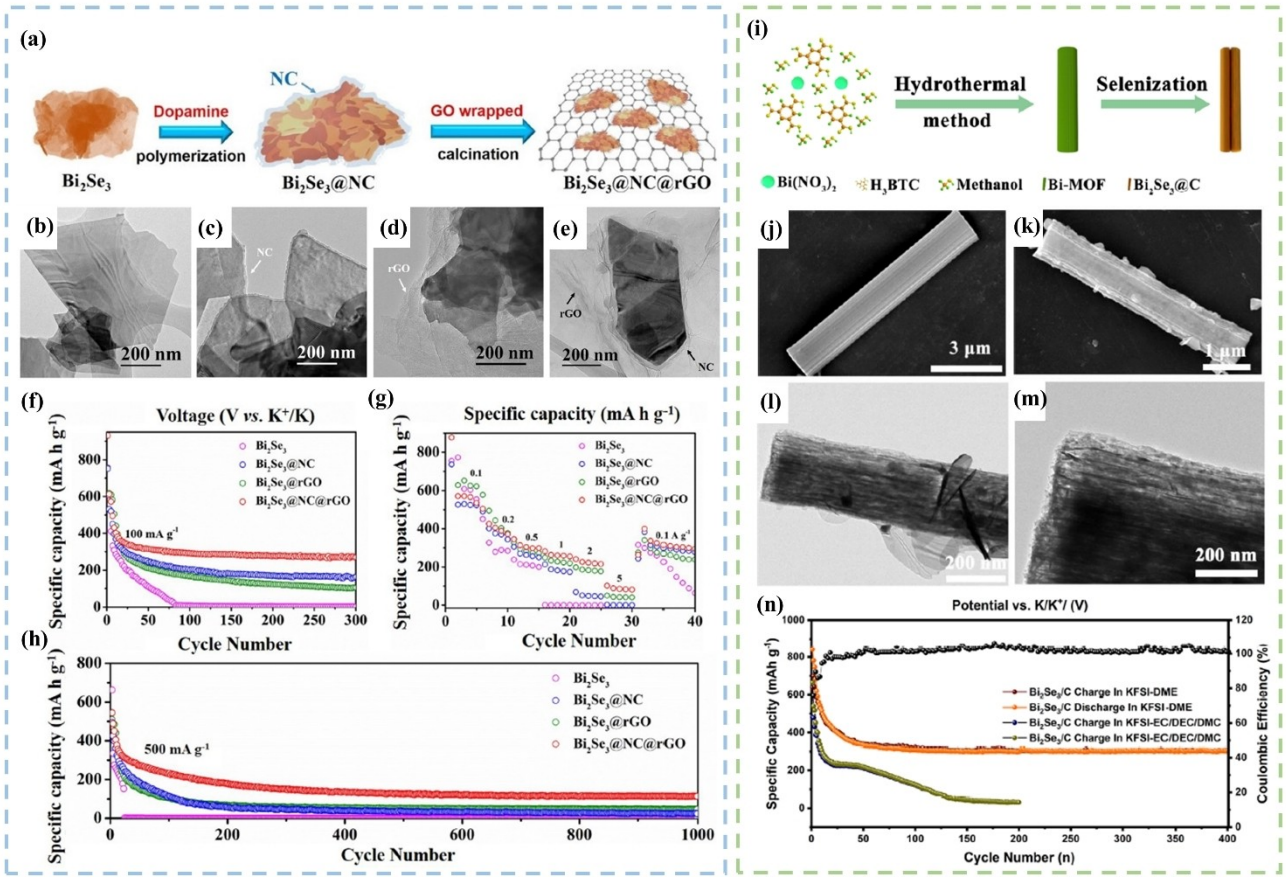

Figure 9. (a) Schematic illustration drawing of the preparation process of triple-layer Bi_2Se_3@NC@rGO composite. TEM images of b) Bi_2Se_3, c) Bi_2Se_3 @NC, d) Bi_2Se_3@rGO and e) Bi_2Se_3@NC@rGO. (f) cycling performance of Bi_2Se_3@NC@rGO at current density of 0.1 A g^{-1} (g) Rate performance of Bi_2Se_3@NC@rGO. (h) cycling performance of Bi_2Se_3@NC@rGO at current density of 0.5 A g^{-1}. Reproduced with permission.[56] Copyright 2021, Elsevier. (i) Schematic diagram for the fabrication process of Bi_2Se_3@C composites. SEM image of (j) Bi-MOFs, (k) Bi_2Se_3@C. (l–m) TEM images of Bi_2Se_3@C. (n) cycling performance of Bi_2Se_3@C. Reproduced with permission.[55] Copyright 2020, American Chemical Society.

Figure 10 e. Therefore, Bi_2Te_3@C can still maintain a reversible capacity of 204 mAh g^{-1} at current density of 1 A g^{-1} for 500 cycles and with a retention rate of 79.8% and having stable charge-discharge curve profile (Figure 10g, h). While in the rate performance test, Bi_2Te_3@C can provided reversible capacity of 220 mAh g^{-1} at the current density of 2 A g^{-1} (Figure 10f).

4. Interaction with electrolytes and metal chalcogenides

Compared to the optimization of active materials, the study of the interaction of electrolyte systems with metal chalcogenide has received less attention. Most of the literature just tested various electrolyte systems and selected the system with better electrochemical performance, but lacked an explanation of the real impact of electrolyte on performance, as shown in Table 1. However, as a bridge between the positive electrode and the negative electrode, the electrolyte has a great impact on the cycle life, reversible capacity, rate performance and safety, especially for Sb- and Bi-based chalcogenides. Due to the huge volume expansion during the charge/discharge process and the shuttle effect caused by polychalcogenides, the optimization of the electrolyte is very important in MCs. In the potassium-sulfur battery, Sun's group reported that a high concentration of ether electrolyte can inhibit the dissolution of potassium polysulfide and promote the complete conversion mechanism.[76] Then Liu *et al.* reported that cobalt monoselenide (CoSe) nanoparticles confined in N-doped carbon nanotubes (CoSe@NCNTs) as PIBs anode material, using 1 M potassium hexafluorophosphate (KPF_6) and potassium bis(fluorosulfonyl)imide (KFSI) as electrolytes in DME and ethylene carbonate (EC)/diethyl carbonate (DEC), respectively (Figure 11a).[77] The experimental results confirmed that 1 M KPF_6 in DME has the better cycle lifespan and electrochemical performance, the reason why KPF_6 in DME has better performance was also calculated by Quantum Chemistry (QC) with g09 Gaussian package (Figure 11b), the calculation results show that the generation potential of DME/$PF6^-$ complex is significantly smaller than that of DME/FSI^- complex, which proves that the 1 M KPF_6 in DME electrolyte system is comparable to that of DME/FSI^- complex. There are more DME(-H) radicals in 1 M KFSI in DME, and DME(–H) radicals will form polyethers around the SEI layer during the charge-

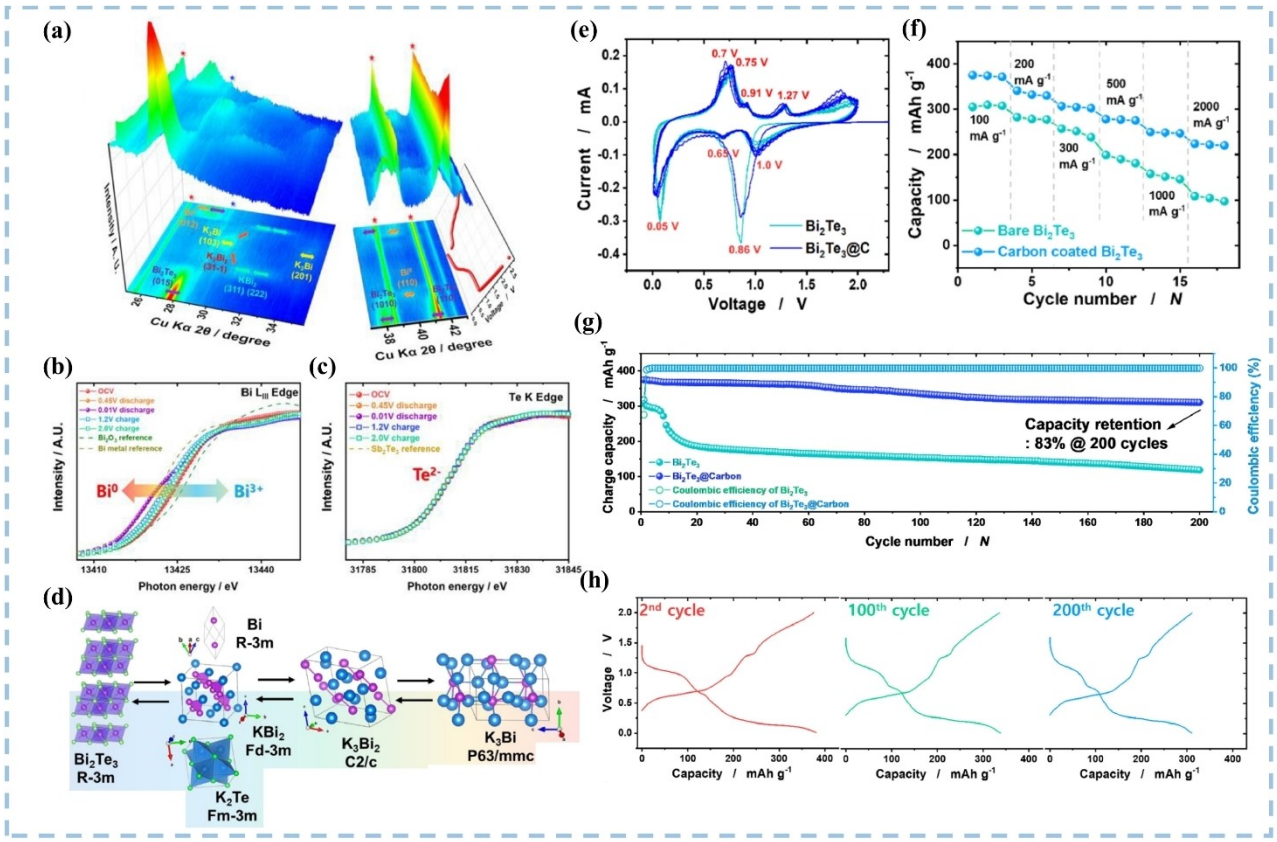

Figure 10. (a) *In-situ* XRD result for Bi_2Te_3@C in PIBs during 1st cycle. XANES result for (b) Bi L3-edge during initial cycle and (c) Te K-edge during initial cycle. (d) Schematic illustration of repetitive electrochemical reaction for Bi_2Te_3@C. (e) CV profile of Bi_2Te_3 and Bi_2Te_3@C. (f) Rate performance of Bi_2Te_3 and Bi_2Te_3@C. (g) Cycling performance of Bi_2Te_3 and Bi_2Te_3@C. (h) Charge discharge curve profile of Bi_2Te_3@C. Reproduced with permission.[59] Copyright 2021, Elsevier.

discharge process, which could prevent the final conversion product of K_2Se dissolved into electrolytes to reach better performance (Figure 11c) Next, Li *et al.* reported $FeSe_2$@rGO as anode material of PIBs, and used 1 M, 5 M KFSI in DME and 1 M KFSI in EC/PC (1 : 1, v/v) marked as EP electrolyte system for testing, respectively.[78] Among them, the 1 M KFSI in DME system observed that the voltage did not reach 3 V during the first charge. It is presumed that the low concentration electrolyte could not inhibit the dissolution of polyselenides. It can be observed that there is a lower average roughness on the surface of the final sheet of the DME system, indicating that this electrolyte system helps to stabilize the charge-discharge process. According to the force-displacement curves, the force response is linear with the displacement, which indicated that the existence of elastic surface of the electrode and Young's modulus value was also calculated to be 5.28 GPa (Figure 11d–g). The existence of an elastic interval will help alleviate the stress change caused by the potassiation/depotassiation process to maintain the integrity of the pole piece (Figure 11h). Therefore, 5 M KFSI in DME obtained more reversible capacity than 1 M KFSI in EP because of the charge-discharge test (Figure 11i). Because of the integrity of the pole piece, a smaller resistance value was observed in the 5 M KFSI in DME electrolyte system in the EIS test after 50 cycles of repeated charge and discharge (Figure 11j). All in all, the higher concentration KFSI ether electrolyte system generally has a good effect on MCs, while in the low concentration electrolyte, the KPF_6 ether electrolyte system achieves better results. In the future, electrolyte system of PIBs anode materials with conversion-alloying dual mechanism should be developed.

5. Summary and outlook

As potassium-ion batteries become a potential candidate for a new generation of the energy storage system, suitable anode materials are being pursued. Among them, MCs have gained enormous attention, especially Sb- and Bi-based chalcogenides, benefiting from the conversion-alloying dual mechanism the large theoretical capacity can be obtained, and extremely high reversible capacity was also obtained in experiments. In this minireview, we summarize the recent progress of Sb- and Bi-based chalcogenides for PIBs, including strategies to improve electrochemical performance and K^+ storage mechanism. Although the prospect of Sb- and Bi-based chalcogenides is promising, the feasibility of practical application is still questioned, and the production cost is greatly increased due to the scarcity of Sb, Bi in the crust. On the other hand, Sb- and Bi-based chalcogenides also face several challenges, such as sluggish kinetics, simultaneously occurring of two reaction

Table 1. Summary of the K^+ storage mechanism and comprehensive performance for Sb-, Bi-based and other chalcogenides.

Sb-based MCs		Stability ($mAh\,g^{-1}$)	Rate ($mAh\,g^{-1}$)	First cycle CE	Electrolytes	Active materials loading	K-ion storage mechanism	Ref
Antimony sulfide (carbon coating)	Sb_2S_3/CNT	212 after 50 cycles @ 0.5 $A\,g^{-1}$	166 @ 1 $A\,g^{-1}$	77.8%	0.8 M KPF_6 in EC/DEC (1 : 1, vol%)	1.5 $mg\,cm^{-2}$	$Sb_2S_3 + xK^+ + xe^- \rightarrow K_xSb_2S_3$ $K_xSb_2S_3 + 2xK^+ + 2xe^- \rightarrow 2Sb + K_xS$ $2Sb + K_xS + (8-3x)K^+ + (8-3x)e^- \rightarrow 2K_3Sb_2 + K_2S_3$	[60]
	Sb_2S_3@C NWs	293 after 50 cycles @ 0.05 $A\,g^{-1}$	163 @ 1 $A\,g^{-1}$	58.4%	1 M KFSI in DME	0.3–0.5 $mg\,cm^{-2}$	$Sb_2S_3 \rightarrow K_xSb_2S_3 \rightarrow K_xS + Sb \rightarrow K_xS + KSb$ $K_xS + KSb \rightarrow K_2S + K_3Sb$	[41]
	Sb_2S_3–rGO	110 after 50 cycles @ 0.05 $A\,g^{-1}$	286 @ 1 $A\,g^{-1}$	51%	1 M KPF_6 in EC/DEC (1 : 1, vol%)	0.7–1.1 $mg\,cm^{-2}$	$Sb_2S_3 + xK^+ + xe^- \leftrightarrow yK_3Sb + zK_2S_3$	[61]
	Sb_2S_3@rGO@NC	89 after 200 cycles @ 0.2 $A\,g^{-1}$	76.7 @ 1 $A\,g^{-1}$	44.1%	1 M KPF_6 in EC/DEC/PC (1 : 1 : 1, vol%)	No provided	$Sb_2S_3 + 6K^+ + 6e^- \rightarrow 3K_2S + 2Sb$ $Sb + K^+ + e^- \rightarrow KSb$ $KSb + 2K^+ + 2e^- \rightarrow K_3Sb$	[42]
	Sb_2S_3@C	295 after 200 cycles @ 1 $A\,g^{-1}$	201 @ 1.6 $A\,g^{-1}$	59.66%	1 M KFSI in EC/DEC (1 : 1, vol%)	0.8 mg	$Sb_2S_3 + K^+ + e^- \rightarrow K_2S_3 + 2Sb$ $Sb + K^+ + e^- \rightarrow KSb$	[62]
Antimony sulfide (conductive polymer coating)	Sb_2S_3@PPy	157 after 50 cycles @ 1 $A\,g^{-1}$	220 @ 2 $A\,g^{-1}$	58%	0.8 M KPF_6 in EC/DEC (1 : 1, vol%)	No provided	No provided	[63]
Antimony sulfide (Others composite)	Ti_3C_2–Sb_2S_3	286 after 500 cycles @ 0.1 $A\,g^{-1}$	102 @ 2 $A\,g^{-1}$	43.3%	3.0 M KFSI in DME	0.6–0.8 $mg\,cm^{-2}$	$Sb_2S_3 + xK^+ + xe^- \rightarrow K_xSb_2S_3$ $K_xSb_2S_3 + 2xK^+ + 2xe^- \rightarrow 2Sb + 3K_xS$ $Sb + 3K_xS + (8-3x)K^+ + (8-3x)e^- \rightarrow 2K_3Sb_2 + K_2S_3$	[43]
	CoS_2/Sb_2S_3@NC/CNT	286 after 500 cycles @ 0.1 $A\,g^{-1}$	454 @ 0.2 $A\,g^{-1}$	66.9%	0.8 M KPF_6 in EC/DEC (1 : 1, vol%)	0.4–0.6 $mg\,cm^{-2}$	No provided	[64]
Antimony selenide (carbon coating)	Sb_2Se_3@rGO@NC	250 after 350 cycles @ 0.5 $A\,g^{-1}$	130 @ 1 $A\,g^{-1}$	77.3%	5 M KFSI in EC/DMC (1 : 1, vol%)	0.6–0.8 $mg\,cm^{-2}$	$4Sb_2Se_3 + 3K^+ + 3e^- \leftrightarrow 3KSb_2Se_4 + 2Sb$ $KSb_2Se_4 + 7K^+ + 7e^- \leftrightarrow 4K_2Se + 2Sb$ $2Sb + xK^+ + xe^- \rightarrow K_xSb_2$ ($x = 1, 2, 2.5,$ and 6) $K_xSb_2 \rightarrow 2Sb + xK^+ + xe^-$ ($x = 1, 2, 2.5,$ and 6)	[49]
	Sb_2Se_3@rGO	203 after 460 cycles @ 0.1 $A\,g^{-1}$	119 @ 2 $A\,g^{-1}$	49%	0.8 M KPF_6 in EC/PC (1 : 1, vol%)	0.8 $mg\,cm^{-2}$	No provided	[48]
	Sb_2Se_3@h-rGO	382 after 500 cycles @ 0.1 $A\,g^{-1}$	73 @ 2 $A\,g^{-1}$	66%	0.8 M KFSI in EC/DEC (1 : 1, vol%)	0.8 mg	No provided	[65]
	C–C/SS	410 after 1000 cycles @ 0.1 $A\,g^{-1}$	73 @ 2 $A\,g^{-1}$	76.9%	3 M KFSI in DEGDME	1.0 $mg\,cm^{-2}$	$4Sb_2Se_3 + 3K^+ + 3e^- \leftrightarrow 3KSb_2Se_4 + 2Sb$ $KSb_2Se_4 + 7K^+ + 7e^- \leftrightarrow 4K_2Se + 2Sb$ $2Sb + xK^+ + xe^- \leftrightarrow K_xSb_2$ ($x = 1, 2, 2.5,$ and 6)	[47]
	Sb_2Se_3@C	191 after 400 cycles @ 0.5 $A\,g^{-1}$	174 @ 2 $A\,g^{-1}$	46%	0.8 M KPF_6 in EC/PC (1 : 1, vol%)	0.8–1.2 $mg\,cm^{-2}$	$Sb_2Se_3 + 12K^+ + 12e^- \leftrightarrow 3K_2Se + 2K_3Sb$	[45]
Antimony selenide (atoms doping)	$(Sb_{0.99}Ni_{0.01})_2Se_3$@C	212 after 250 cycles @ 1 $A\,g^{-1}$	140 @ 10 $A\,g^{-1}$	64.7%	4 M KFSI in DME	0.8–1.0 $mg\,cm^{-2}$	$Sb_2Se_3 + 3K^+ + 3e^- \rightarrow 3K_3SbSe_3 + Sb$ $K_3SbSe_3 + 3K^+ + 3e^- \leftrightarrow 3K_2Se + Sb$ $Sb + xK^+ + xe^- \leftrightarrow K_xSb$ $K_xSb + (3-x)K^+ + 3e^- \leftrightarrow K_3Sb$	[46]
Bismuth sulfide (carbon coating)	NGBS composites	332 after 500 cycles @ 5 $A\,g^{-1}$	328 @ 10 $A\,g^{-1}$	83%	1 M KPF_6 in DME	1.0 $mg\,cm^{-2}$	$Bi_2S_3 + xK^+ + xe^- \leftrightarrow K_xBi_2S_3$ $K_xBi_2S_3 + (6-x)K^+ + (6-x)xe^- \rightarrow 3K_2S + 2Bi$ $Bi + xK^+ + xe^- \leftrightarrow K_xBi$ $3K_2S + 2Bi \rightarrow (1-y)K_xBi_2S_3 + 3yS + 2yBi + (6-x(1-y))(K^+ + e^-)$	[52]
	Bi_2S_3@SC	200 after 250 cycles @ 0.5 $A\,g^{-1}$	269 @ 1 $A\,g^{-1}$	62.3%	1 M KFSI in EC/DEC (1 : 1, vol%)	3.0 $mg\,cm^{-2}$	No provided	[54]

ACES Asian Chemical Editorial Society
CHEMISTRY AN ASIAN JOURNAL Review

Table 1. continued

Sb-based MCs		Stability ($mAh\,g^{-1}$)	Rate ($mAh\,g^{-1}$)	First cycle CE	Electrolytes	Active materials loading	K-ion storage mechanism	Ref
	Bi_2S_3-CNT	210 after 50 cycles @ $0.2\,A\,g^{-1}$	No provided	79%	Not provided	No provided	$Bi_2S_3 + 6K \rightarrow 2Bi + 3K_2S$ $Bi + 3K \rightarrow K_3Bi$ $Bi + K \rightarrow KBi$	[51]
	Bi_2S_3@rGO	200 after 1200 cycles @ $0.1\,A\,g^{-1}$	261 @ $0.3\,A\,g^{-1}$	61.91%	Concentrated KTFSI in DEGDME	1–2 $mg\,cm^{-2}$	No provided	[66]
	Bi_2S_3@RGO	237 after 300 cycles @ $2\,A\,g^{-1}$	250 @ $0.3\,A\,g^{-1}$	85.2%	1 M KPF_6 in DME	1.0–1.2 $mg\,cm^{-2}$	$Bi_2S_3 \leftrightarrow KBiS_2$ $KBiS_2 \leftrightarrow Bi \rightarrow KBi_2 \rightarrow K_3Bi$	[53]
Bismuth selenide (Carbon coating)	Bi_2Se_3@NC@rGO	114 after 1000 cycles @ $0.5\,A\,g^{-1}$	102 @ $5\,A\,g^{-1}$	65.7%	0.8 M KPF_6 in EC/DEC (1 : 1, vol%)	1.0 $mg\,cm^{-2}$	$Bi_2Se_3 + 3K^+ + 3e^- \leftrightarrow Bi + K_3BiSe_3$ $K_3BiSe_3 + 3K^+ + 3e^- \leftrightarrow Bi + K_2Se$ $2Bi + 3K^+ + e^- \leftrightarrow KBi_2KBi_2 + 5K^+ + 5e^- \leftrightarrow K_3Bi$	[56]
	Bi_2Se_3 (Bi-MOF derive)	543 after 5000 cycles @ $1\,A\,g^{-1}$	304 @ $2\,A\,g^{-1}$	68%	3.0 M KFSI in DME	1.0–1.2 $mg\,cm^{-2}$	$Bi_2Se_3 + 6K^+ + 6e^- \leftrightarrow 2Bi + 3K_2Se$ $Bi + 3K^+ + 3e^- \leftrightarrow K_3Bi$	[55]
	Bi_2Se_3 (glucose derive)	214 after 1000 cycles @ $1\,A\,g^{-1}$	210 @ $2\,A\,g^{-1}$	74%	2 M KFSI in EC/DEC (1 : 1, vol%)	1.0 mg	$Bi_2Se_3 + 6K^+ + 6e^- \leftrightarrow 2Bi + 3K_2Se$ $Bi + 3K^+ + 3e^- \leftrightarrow K_3Bi$	[57]
	Bi_2Se_3 @NC	131 after 2000 cycles @ $1\,A\,g^{-1}$	195 @ $0.3\,A\,g^{-1}$	72.58%	5 M KFSI in DEGDME	1.0-1.5 $mg\,cm^{-2}$	$Bi_2Se_3 + K^+ + e^- \leftrightarrow Bi + KBi_2 + K_2Se$ $Bi + KBi_2 + K^+ + e^- \leftrightarrow K_3Bi$	[67]
Bismuth telluride (carbon coating)	Bi_2Te_3@C	204 after 500 cycles @ $1\,A\,g^{-1}$	220 @ $2\,A\,g^{-1}$	78%	0.5 M KFSI in EC/DMC (1 : 1, vol%)	3.0 mg	$Bi_2Te_3 + 6K^+ + 6e^- \leftrightarrow 3K_2Te + 2Bi^0$ $2Bi^0 + 3K^+ + e^- \leftrightarrow KBi_2$ $KBi_2 + 2K^+ + 2e^- \leftrightarrow K_3Bi_2$ $K_3Bi_2 + 3K^+ + 3e^- \leftrightarrow 2K_3Bi$	[59]
Other MCs	SnS_2@C	183 after 1000 cycles @ $2\,A\,g^{-1}$	219.4 @ $5\,A\,g^{-1}$	59.5%	0.8 M KPF_6 in EC/DEC (1 : 1, vol%)	1.0–1.2 $mg\,cm^{-2}$	$SnS_2 \leftrightarrow SnS \leftrightarrow K_4Sn_{23} + K_2S_5 \leftrightarrow KSn + K_2S$	[68]
	SnSe@C	203 after 1000 cycles @ $0.5\,A\,g^{-1}$	135.2 @ $1.2\,A\,g^{-1}$	59.2%	1 M KFSI in EC/DEC (1 : 1, vol%)	1.1 $mg\,cm^{-2}$	$SnSe \leftrightarrow Sn + K_2Se_5 \leftrightarrow K_4Sn_{23} + K_2Se_5$	[69]
	V_3S_4@NCNF	245 after 1000 cycles @ $2\,A\,g^{-1}$	202 @ $10\,A\,g^{-1}$	62%	3.0 M KFSI in DME	0.8 $mg\,cm^{-2}$	No provided	[70]
	V_3Se_4/NPCNFs	207 after 800 cycles @ $2\,A\,g^{-1}$	185 @ $5\,A\,g^{-1}$	54%	3.0 M KFSI in DME	1.0–1.2 mg cm^{-2}	No provided	[71]
	MoS_2/MXene	206 after 100 cycles @ $0.05\,A\,g^{-1}$	168 @ $0.5\,A\,g^{-1}$	66.5%	0.8 M KPF_6 in EC/DEC (1 : 1, vol%)	No provided	$MoS_2 + xK^+ + xe^- \leftrightarrow K_xMoS_2$ $K_xMoS_2 + (4-x)K^+ + (4-x)e^- \leftrightarrow Mo + 2K_2S$	[72]
	$MoSe_2$/N,P–C@N–C⊂$MoSe_2$	217 after 500 cycles @ $1\,A\,g^{-1}$	187 @ $5\,A\,g^{-1}$	49.8%	1 M KFSI in EC/DEC (1 : 1, vol%)	No provided	No provided	[73]
	ZnS@C	211 after 5700 cycles @ $1\,A\,g^{-1}$	225 @ $1.6\,A\,g^{-1}$	45.2%	3.0 M KTFSI in DME	0.7–1.1 $mg\,cm^{-2}$	$ZnS + 2K^+ + 2e^- \leftrightarrow K_2S + Zn$ $13Zn + K^+ + e^- \leftrightarrow KZn_{13}$	[74]
	ZnSe@PCNF	270 after 1000 cycles @ $0.5\,A\,g^{-1}$	158 @ $2\,A\,g^{-1}$	66%	3.0 M KTFSI in DEGDME	0.25 $mg\,cm^{-2}$	No provided	[75]

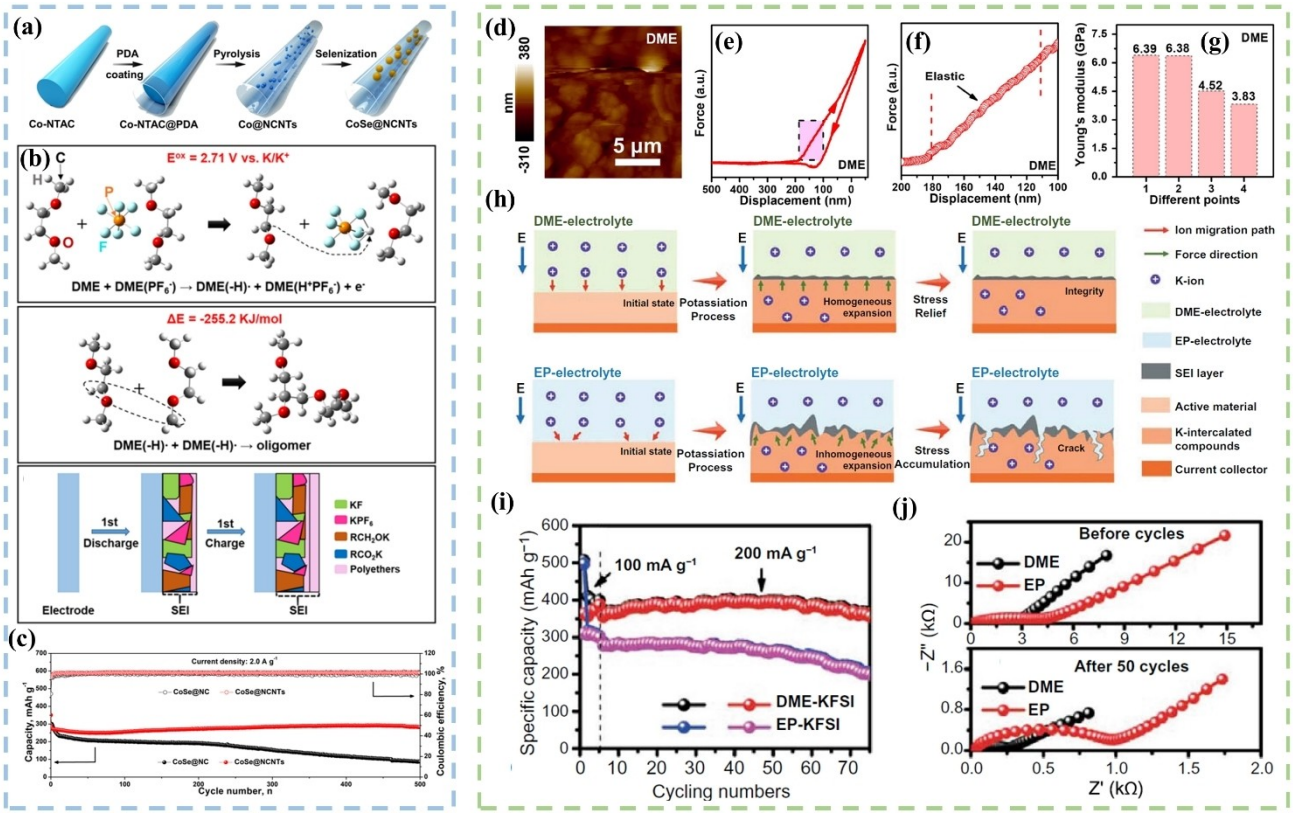

Figure 11. (a) Schematic illustration of the synthesis of CoSe@NCNTs. (b) Selected results of quantum chemistry calculations: DME oxidation with $PF6^-$ anion. (c) cycling performance of CoSe@NCNTs. Reproduced with permission.[77] Copyright 2021, American Chemical Society. (d) AFM images, (e) Representative force-displacement curves, (f) A detailed force analysis of SEI layers, (g) Young's modulus of $FeSe_2$@RGO electrode using a DME-based electrolyte. (h) Schematic illustration of expansion process of electrodes in DME- and EP-based electrolyte. (i) cycling stability of $FeSe_2$@RGO electrode in DME- and EP-based electrolyte. EIS spectra of $FeSe_2$@RGO electrode with DME-based and EP-based electrolytes (j) before and (k) after 50 cycles. Reproduced from Ref.,[78] under the terms of the CC BY 4.0 license.

mechanisms due to the conversion-alloying dual mechanism, and the huge volume expansion caused by the alloying reaction and the polychalcogenides-induced shuttle effect caused by conversion reaction. Therefore, various methods were developed to optimize the stability of Sb- and Bi-based chalcogenides during K^+ storage, such as the most common carbon coating method, which uses dopamine, PPy or rGO to coat different properties of carbon layers on active materials, core-shell structure or surface chemical bond modification, etc., leading to significant improvement in electrochemical performance, and have achieved good performance improvement in in single alloying/conversion reaction anode materials. However, these strategies still have issues worth raising for discussion. In our opinion, the following research directions should be emphasized:

1. The investigation of Sb_2Te_3 in PIBs need to further conduct. Sb_2Te_3 has a high theoretical volumetric capacity, which is potential high energy consuming device anode material, but there is no literature report on its electrochemical performance and K^+ storage mechanism.

2. Build heterostructures and study interactions with other materials after reaction with K^+. Rational design of heterostructures can improve electron and ion transport. However, the phase change of active materials occurs when K^+ is inserted/extracted, and most of the current literature does not consider the phase transition after electrochemical reaction when simulating and characterizing the advantages of their materials.

3. The interface between active materials and electrolytes should be clarified. For the same active materials, the electrical performance are poles apart, which indicates SEI layer will largely affect structure and cycle stability. Especially to active materials which undergo alloy-conversion dual mechanism, not only need to stabilize SEI layer, but also inhibit polychalcogenides dissolution. Thus, deep insight into electrolyte is important to attain high performance Sb- and Bi-based chalcogenides PIB anode.

4. Investigate the K^+ storage mechanism of Sb- and Bi-based chalcogenides using multi-detection methods. Knowing the properties of the intermediate products can give great inspiration to the design of the anode structure. Since the two reaction mechanisms have very different properties for crystallinity. The *in-situ* XRD is a powerful method to reveal the crystalline intermediate products caused by the alloying reaction, but the chalcogens conversion reaction is usually produced in an amorphous state, so it needs to rely on vibrational spectroscopy or mass spectrometry to detect. In

most of literature, amorphous chalcogens conversion reaction is lack of detailed analysis.

5. DFT simulation should be proposed to verify the advantages of the proposed electrochemical model. The theoretical calculation of interaction between active materials and K^+ could point out the origin of advantages provide better design guidelines and electrolyte composition of Sb- and Bi-based chalcogenides PIBs anode.

All in all, based on the in-depth investigation of the interaction between active materials and K^+, it is believed that the challenges faced by Sb- and Bi-based chalcogenides will be overcome, and it is hoped that this review can provide researchers with Sb- and Bi-based chalcogenides anode structure design and guidelines for mechanism derivation.

6. Notes

The authors declare no competing financial interest.

Acknowledgment

This work received financial support from the 2030 Cross-Generation Young Scholars Program by Ministry of Science and Technology, Taiwan (MOST 110-2628-E-007-001). H.-Y.T. also acknowledges the financial support of National Tsing Hua University, Taiwan, through Grant No. 109QI030E1.

Conflict of Interest

The authors declare no conflict of interest.

Keywords: potassium ion batteries · antimony · bismuth · chalcogenides · mechanism

[1] A. Barré, B. Deguilhem, S. Grolleau, M. Gérard, F. Suard, D. Riu, *J. Power Sources* **2013**, *241*, 680–689.
[2] L. Lu, X. Han, J. Li, J. Hua, M. Ouyang, *J. Power Sources* **2013**, *226*, 272–288.
[3] G. Zubi, R. Dufo-López, M. Carvalho, G. Pasaoglu, *Renewable Sustainable Energy Rev.* **2018**, *89*, 292–308.
[4] J. C. Pramudita, D. Sehrawat, D. Goonetilleke, N. Sharma, *Adv. Energy Mater.* **2017**, *7* (24), 1602911.
[5] D. Li, Y. Zhang, Q. Sun, S. Zhang, Z. Wang, Z. Liang, P. Si, L. Ci, *Energy Storage Mater.* **2019**, *23*, 367–374.
[6] X. Wu, D. P. Leonard, X. Ji, *Chem. Mater.* **2017**, *29* (12), 5031–5042.
[7] M. Zhou, P. Bai, X. Ji, J. Yang, C. Wang, Y. Xu, *Adv. Mater.* **2021**, *33* (7), 2003741.
[8] L. Fan, R. Ma, Q. Zhang, X. Jia, B. Lu, *Angew. Chem.* **2019**, *131* (31), 10610–10615.
[9] L. Wang, J. Yang, J. Li, T. Chen, S. Chen, Z. Wu, J. Qiu, B. Wang, P. Gao, X. Niu, *J. Power Sources* **2019**, *409*, 24–30.
[10] X. Min, J. Xiao, M. Fang, W. A. Wang, Y. Zhao, Y. Liu, A. M. Abdelkader, K. Xi, R. V. Kumar, Z. Huang, *Energy Environ. Sci.* **2021**, *14* (4), 2186–2243.
[11] Y.-Y. Hsieh, K.-T. Chen, H.-Y. Tuan, *Chem. Eng. J.* **2021**, *420*, 130451.
[12] K.-T. Chen, H.-Y. Tuan, *ACS Nano* **2020**, *14* (9), 11648–11661.
[13] C.-H. Chang, K.-T. Chen, Y.-Y. Hsieh, C.-B. Chang, H.-Y. Tuan, *ACS Nano* **2022**, **16**, **1486-1501**.
[14] C.-B. Chang, K.-T. Chen, H.-Y. Tuan, *J. Colloid Interface Sci.* **2022**, *608*, 984–994.
[15] C.-Y. Tsai, C.-H. Chang, T.-L. Kao, K.-T. Chen, H.-Y. Tuan, *Chem. Eng. J.* **2021**, *417*, 128552.
[16] S.-B. Huang, Y.-Y. Hsieh, K.-T. Chen, H.-Y. Tuan, *Chem. Eng. J.* **2021**, *416*, 127697.
[17] Z. Li, R. Sun, Z. Qin, X. Liu, C. Wang, H. Fan, Y. Zhang, S. Lu, *Mater. Chem. Front.* **2021**, *5* (12), 4401–4423.
[18] H. Tan, Y. Feng, X. Rui, Y. Yu, S. Huang, *Small Methods* **2020**, *4* (1), 1900563.
[19] J. Zhou, Y. Liu, S. Zhang, T. Zhou, Z. Guo, *InfoMat* **2020**, *2* (3), 437–465.
[20] M. Aydinol, A. Kohan, G. Ceder, K. Cho, J. Joannopoulos, *Phys. Rev. B* **1997**, *56* (3), 1354.
[21] Y. Guo, T. Park, J. W. Yi, J. Henzie, J. Kim, Z. Wang, B. Jiang, Y. Bando, Y. Sugahara, J. Tang, *Adv. Mater.* **2019**, *31* (17), 1807134.
[22] W. Zhao, S. Yuan, L. Zhang, F. Jiang, Y. Yang, G. Zou, H. Hou, P. Ge, W. Sun, X. Ji, *Energy Storage Mater.* **2022**, *45*, 1183–1200.
[23] X. Huang, J. Sun, L. Wang, X. Tong, S. X. Dou, Z. M. Wang, *Small* **2021**, *17* (6), 2004369.
[24] L. Lin, W. Lei, S. Zhang, Y. Liu, G. G. Wallace, J. Chen, *Energy Storage Mater.* **2019**, *19*, 408–423.
[25] M. Pumera, Z. Sofer, A. Ambrosi, *J. Mater. Chem. A* **2014**, *2* (24), 8981–8987.
[26] J. Cao, J. Li, D. Li, Z. Yuan, Y. Zhang, V. Shulga, Z. Sun, W. Han, *Nano-Micro Lett.* **2021**, *13* (1), 1–20.
[27] X. Zuo, J. Zhu, P. Müller-Buschbaum, Y.-J. Cheng, *Nano Energy* **2017**, *31*, 113–143.
[28] J. He, Y. Wei, T. Zhai, H. Li, *Mater. Chem. Front.* **2018**, *2* (3), 437–455.
[29] W.-C. Chang, K.-W. Tseng, H.-Y. Tuan, *Nano Lett.* **2017**, *17* (2), 1240–1247.
[30] W. Hong, P. Ge, Y. Jiang, L. Yang, Y. Tian, G. Zou, X. Cao, H. Hou, X. Ji, *ACS Appl. Mater. Interfaces* **2019**, *11* (11), 10829–10840.
[31] I. Sultana, M. M. Rahman, T. Ramireddy, Y. Chen, A. M. Glushenkov, *J. Mater. Chem. A* **2017**, *5* (45), 23506–23512.
[32] S. Yu, S. O. Kim, H. S. Kim, W. Choi, *Int. J. Energy Res.* **2019**, *43* (13), 7646–7654.
[33] K.-T. Chen, Y.-C. Yang, L.-M. Lyu, M.-Y. Lu, H.-Y. Tuan, *Nano Energy* **2021**, *88*, 106233.
[34] I. Sultana, M. M. Rahman, Y. Chen, A. M. Glushenkov, *Adv. Funct. Mater.* **2018**, *28* (5), 1703857.
[35] W. C. Chang, J. H. Wu, K. T. Chen, H. Y. Tuan, *Adv. Sci.* **2019**, *6* (9), 1801354.
[36] V. R. C. Thanu, M. Jayakumar, *Sep. Purif. Technol.* **2020**, *235*, 116169.
[37] J. Zhang, L. Lai, H. Wang, M. Chen, Z. X. Shen, *Mater. Today* **2021**, *21*, 100747.
[38] T. Xiong, Y. Wang, B. Yin, W. Shi, W. S. V. Lee, J. Xue, *Nano-Micro Lett.* **2020**, *12* (1), 1–9.
[39] S. Zhao, J. Li, H. Chen, J. Zhang, *J. Electrochem. Energy Convers. Storage* **2020**, *17* (3), 031010.
[40] Y. Liu, Z. Tai, J. Zhang, W. K. Pang, Q. Zhang, H. Feng, K. Konstantinov, Z. Guo, H. K. Liu, *Nat. Commun.* **2018**, *9* (1), 1–10.
[41] Y. Cheng, Z. Yao, Q. Zhang, J. Chen, W. Ye, S. Zhou, H. Liu, M.-S. Wang, *Adv. Funct. Mater.* **2020**, *30* (52), 2005417.
[42] S. Chong, S. Qiao, X. Wei, T. Li, L. Yuan, S. Dong, W. Huang, *iScience* **2021**, *24* (12), 103494.
[43] T. Wang, D. Shen, H. Liu, H. Chen, Q. Liu, B. Lu, *ACS Appl. Mater. Interfaces* **2020**, **12**, **57907-57915**.
[44] Y. Shi, F. Li, Y. Zhang, L. He, Q. Ai, W. Luo, *Nanomaterials* **2019**, *9* (4), 560.
[45] Z. Yi, Y. Qian, J. Tian, K. Shen, N. Lin, Y. Qian, *J. Mater. Chem. A* **2019**, *7* (19), 12283–12291.
[46] B. Sheng, L. Wang, H. Huang, H. Yang, R. Xu, X. Wu, Y. Yu, *Small* **2020**, *16* (49), 2005272.
[47] L. Guo, L. Cao, J. Huang, J. Li, K. Kajiyoshi, J. He, H. Qi, *ACS Appl. Energ. Mater.* **2021**, *4* (9), 10391–10403.
[48] Z. Yi, Y. Qian, S. Jiang, Y. Li, N. Lin, Y. Qian, *Chem. Eng. J.* **2020**, *379*, 122352.
[49] S. Wang, P. Xiong, X. Guo, J. Zhang, X. Gao, F. Zhang, X. Tang, P. H. L. Notten, G. Wang, *Adv. Funct. Mater.* **2020**, *30* (27), 2001588.
[50] S. Dong, D. Yu, J. Yang, L. Jiang, J. Wang, L. Cheng, Y. Zhou, H. Yue, H. Wang, L. Guo, *Adv. Mater.* **2020**, *32* (23), 1908027.
[51] J.-Y. Hwang, R. Kumar, H. M. Kim, M. H. Alfaruqi, J. Kim, Y.-K. Sun, *RSC Adv.* **2020**, *10* (11), 6536–6539.
[52] C. Shen, G. Song, X. Zhu, D. Wang, L. Huang, Z. Sun, Y. Wu, *Nano Energy* **2020**, *78*, 105294.

[53] Y. Liu, M. Li, Y. Zheng, H. Lin, Z. Wang, W. Xin, C. Wang, F. Du, *Nanoscale* **2020**, *12* (48), 24394–24402.
[54] C. Wang, J. Lu, H. Tong, S. Wu, D. Wang, B. Liu, L. Cheng, Z. Lin, L. Hu, H. Wang, W. Zhang, Q. Chen, *Nano Res.* **2021**, *14* (10), 3545–3551.
[55] T. Yang, J. Liu, D. Yang, Q. Mao, J. Zhong, Y. Yuan, X. Li, X. Zheng, Z. Ji, H. Liu, G. Wang, R. Zheng, *ACS Appl. Energ. Mater.* **2020**, *3* (11), 11073–11081.
[56] K.-T. Chen, S. Chong, L. Yuan, Y.-C. Yang, H.-Y. Tuan, *Energy Storage Mater.* **2021**, *39*, 239–249.
[57] X. Zhao, C. Zhang, G. Yang, Y. Wu, Q. Fu, H. Zhao, Y. Lei, *Inorg. Chem. Front.* **2021**, *8* (18), 4267–4275.
[58] C. H. Gillard, P. P. Jana, A. Rawal, N. Sharma, *J. Alloys Compd.* **2021**, *854*, 155621.
[59] J. K. Ko, J. H. Jo, H. J. Kim, J. S. Park, H. Yashiro, N. Voronina, S.-T. Myung, *Energy Storage Mater.* **2021**, *43*, 411–421.
[60] M. Li, F. Huang, J. Pan, L. Li, Y. Zhang, Q. Yao, H. Zhou, J. Deng, *Nanomaterials* **2019**, *9* (9), 1323.
[61] V. Lakshmi, A. A. Mikhaylov, A. G. Medvedev, C. Zhang, T. Ramireddy, M. M. Rahman, P. Cizek, D. Golberg, Y. Chen, O. Lev, P. V. Prikhodchenko, A. M. Glushenkov, *J. Mater. Chem. A* **2020**, *8* (22), 11424–11434.
[62] L. Yang, W. Hong, Y. Tian, G. Zou, H. Hou, W. Sun, X. Ji, *Chem. Eng. J.* **2020**, *385*, 123838.
[63] Y. Shi, F. Li, Y. Zhang, L. He, Q. Ai, W. Luo, *Nanomaterials* **2019**, *9* (4), 560.
[64] X. Li, H. Liang, X. Liu, R. Sun, Z. Qin, H. Fan, Y. Zhang, *Chem. Eng. J.* **2021**, *425*, 130657.
[65] Z. Yang, W. Li, G. Zhang, J. Wang, J. Zuo, Q. Xu, H. Shan, X. He, M. Lv, J. Hu, W. Huang, J. Zhang, X. Li, *Nano Energy* **2022**, *93*, 106764.
[66] X. Sun, L. Wang, C. Li, D. Wang, I. Sikandar, R. Man, F. Tian, Y. Qian, L. Xu, *Nano Res.* **2021**, *14* (12), 4696–4703.
[67] X. Sun, B. Zhang, M. Chen, L. Wang, D. Wang, R. Man, S. Iqbal, F. Tian, Y. Qian, L. Xu, *Nano Today* **2022**, *43*, 101408.
[68] D. Li, L. Dai, X. Ren, F. Ji, Q. Sun, Y. Zhang, L. Ci, *Energy Environ. Sci.* **2021**, *14* (1), 424–436.
[69] R. Verma, P. N. Didwal, A.-G. Nguyen, C.-J. Park, *Chem. Eng. J.* **2021**, *421*, 129988.
[70] D. Wu, W. Zhang, Y. Feng, J. Ma, *J. Mater. Chem. A* **2020**, *8* (5), 2618–2626.
[71] L. Xu, W. Guo, L. Zeng, X. Xia, Y. Wang, P. Xiong, Q. Chen, J. Zhang, M. Wei, Q. Qian, *Chem. Eng. J.* **2021**, *419*, 129607.
[72] J. Li, B. Rui, W. Wei, P. Nie, L. Chang, Z. Le, M. Liu, H. Wang, L. Wang, X. Zhang, *J. Power Sources* **2020**, *449*, 227481.
[73] X. Wang, W. Kang, Y. Wang, B. Zhang, D. Sun, *J. Mater. Chem. A* **2021**, *9* (33), 17780–17789.
[74] X. Xu, F. Li, D. Zhang, Z. Liu, S. Zuo, Z. Zeng, J. Liu, *Adv. Sci.* **2022**, 9, 2200247.
[75] J. H. Na, Y. C. Kang, S.-K. Park, *Chem. Eng. J.* **2021**, *425*, 131651.
[76] L. Wang, J. Bao, Q. Liu, C.-F. Sun, *Energy Storage Mater.* **2019**, *18*, 470–475.
[77] Y. Liu, Q. Deng, Y. Li, Y. Li, W. Zhong, J. Hu, X. Ji, C. Yang, Z. Lin, K. Huang, *ACS Nano* **2021**, *15* (1), 1121–1132.
[78] X. Li, J. Li, W. Zhuo, Z. Li, L. Ma, Z. Ji, L. Pan, W. Mai, *Nano-Micro Lett.* **2021**, *13* (1), 179.

Manuscript received: February 22, 2022
Revised manuscript received: April 14, 2022
Accepted manuscript online: April 20, 2022
Version of record online: May 11, 2022